

Direct measurement of the  $\bar{K}N \rightarrow \pi\Sigma$  scattering amplitude below the  $\bar{K}N$  threshold employing the  $d(K^-, N)\pi\Sigma^-$  reaction

Kentaro Inoue

October 30, 2022

# Contents

<b>1</b>	<b>Introduction</b>	<b>5</b>
1.1	Discovery of the $\Lambda(1405)$ . . . . .	5
1.2	Recent situation of $\Lambda(1405)$ . . . . .	5
1.3	$\bar{K}N$ interaction and $\Lambda(1405)$ . . . . .	6
1.4	$d(K^-, n)$ reaction . . . . .	6
<b>2</b>	<b>Experimental setup</b>	<b>10</b>
2.1	Experimental facility . . . . .	10
2.1.1	J-PARC . . . . .	10
2.1.2	K1.8BR beam line . . . . .	11
2.2	Beam line detectors . . . . .	14
2.2.1	Overview . . . . .	14
2.2.2	Beam momentum analyzer . . . . .	15
2.2.3	BPD . . . . .	16
2.2.4	Vertex chamber - BPC . . . . .	16
2.2.5	Beam definition counter . . . . .	17
2.3	Target system . . . . .	17
2.3.1	Luquid $D_2$ target system . . . . .	17
2.4	The cylindrical detector system . . . . .	19
2.4.1	Solenoid magnet . . . . .	19
2.4.2	Cylindrical drift chamber . . . . .	20
2.4.3	Cylindrical detector hodoscope . . . . .	21
2.4.4	Inner hodoscope . . . . .	22
2.5	Forward detector systems . . . . .	22
2.5.1	Beam sweeping magnet . . . . .	23
2.5.2	Beam veto counter . . . . .	23
2.5.3	Neutron counter array . . . . .	23
2.5.4	Charge veto counter . . . . .	24
2.5.5	Proton counter . . . . .	24
2.5.6	Forward drift chamber . . . . .	24
2.6	Data acquisition system . . . . .	24
2.6.1	Overall system . . . . .	24
2.6.2	Trigger circuit . . . . .	26

<b>CONTENTS</b>	<b>3</b>
<b>3 Data analysis</b>	<b>28</b>
3.1 Over view . . . . .	28
3.1.1 Basical calibration . . . . .	29
3.2 Beam line . . . . .	30
3.2.1 DAQ live rate and trigger efficiency . . . . .	30
3.2.2 T0 and BHD aanalysis . . . . .	33
3.2.3 Beam line chamger . . . . .	33
3.2.4 Beam momentum analyzer - D5 magnet . . . . .	35
3.2.5 BLC2-BPC matching . . . . .	36
3.2.6 Luminosity . . . . .	37
3.3 CDS . . . . .	38
3.3.1 CDC tracking . . . . .	39
3.3.2 CDH . . . . .	40
3.3.3 Vertex reconstruction . . . . .	41
3.3.4 Particle identification . . . . .	41
3.3.5 Time walk corrlction of CDC . . . . .	43
3.3.6 Recunstructed hyperons by CDS . . . . .	43
3.3.7 CDC efficeicny . . . . .	43
3.4 Forward proton detectors . . . . .	45
3.4.1 Forward charge praticle identification . . . . .	45
3.4.2 Time offset turning . . . . .	47
3.4.3 Horizontal axis accuracy by the $d(K^-, (\Lambda\pi^-)_{CDS})''p''$ events . . . . .	47
3.4.4 Forward proton efficiency . . . . .	50
3.5 Forward neutron detector system . . . . .	52
3.5.1 Neutron Counter . . . . .	52
3.5.2 NC efficiency estimation . . . . .	54
3.5.3 Neutron overkill by the BVC/CVC . . . . .	58
<b>4 Discussion</b>	<b>60</b>
4.1 $\pi\Sigma$ spectra . . . . .	60
4.1.1 Mode decomposition of $d(K^-, p)$ . . . . .	60
4.1.2 Mode decomposition of $d(K^-, n)$ . . . . .	61
4.2 Comparison with DCC model . . . . .	64
4.3 Demonstration of fitting by DCC models . . . . .	65
<b>5 Conclusion</b>	<b>69</b>
<b>A Offline selection</b>	<b>71</b>
A.1 $d(K^-, n\pi^+\pi^-)$ . . . . .	71
A.2 $d(K^-, p\pi^-\pi^-)$ . . . . .	72
<b>B Geant4 simulation</b>	<b>73</b>

<b>C</b>	$K^- d \rightarrow K^0 nn$ events	<b>77</b>
<b>D</b>	$d(K^-, p)''\pi^-\Lambda''/\pi^-\Sigma^0''$ mode	<b>79</b>

# Chapter 1

## Introduction

### 1.1 Discovery of the $\Lambda(1405)$

The  $\Lambda(1405)$  is a hyperon resonance state with strangeness  $S = -1$ , isospin  $I = 0$  spin-parity  $J^P = \frac{1}{2}^-$ . This resonance state was first predicted by Dalitz and Tuan [1] in 1959. They analyzed the  $\bar{K}N$  scattering data and found that the  $I = 0$   $\bar{K}N$  scattering amplitude has a resonance pole below the  $\bar{K}N$  mass threshold. They suggested that this resonance pole is a bound state of  $\bar{K}N$  [3]. Later,  $\Lambda(1405)$  was first reported in a hydrogen bubble chamber experiment at the Lawrence Radiation Laboratory: the  $K^- p \rightarrow \Sigma\pi\pi\pi$  reaction with a  $K^-$  beam of  $1.15\text{GeV}/c$ .

A high-statistics generation experiment of  $\Lambda(1405)$  was performed at CERN [4]. In this experiment,  $K^- p \rightarrow \Sigma^+(1660)\pi^- \rightarrow \Lambda(1405)\pi^+\pi^-$  reaction was measured using a  $4.2\text{GeV}/c$   $K^-$  beam. Dalitz and Deloff deduced mass  $M = 1406.5 \pm 4.0 \text{ MeV}/c^2$  and width  $\Gamma = 50 \pm 2.0 \text{ MeV}/c^2$  of  $\Lambda(1405)$  from fitting of this data. In the latest Particle Data Group, the mass of *Lambda*(1405) was determined to be  $M = 1405.1^{+1.3}_{-1.0}\text{MeV}/c^2$  and *Gamma* =  $50\text{GeV}/c^2$  from these analyses. This method of analysis is called the phenomenological method.

### 1.2 Recent situation of $\Lambda(1405)$

Wise et al. confirmed that the  $\Lambda(1405)$  resonance pole is located below the  $\bar{K}N$  threshold using a chiral Lagrangian with a strangeness  $S = -1$  sector [20]. In the 2000's, the chiral unitary model proposed that  $\Lambda(1405)$  is a dynamical generated molecular state consisting of two poles [21]. The higher pole is coupled to the  $\bar{K}N$  channel, while the lower pole is coupled to the  $\pi\sigma$  channel. Therefore, they claim that the pole coupled to  $\bar{K}N$  shifts to a higher position than the previously mentioned  $1405 \text{ MeV}/c$ .

Photoproduction of  $\Lambda(1405)$  was performed at LEPS in Spring-8. In that experiment, the  $\gamma p \rightarrow K^+\Lambda(1405)$  reaction at  $E_\gamma = 1.5 - 2.4\text{GeV}$  was

used to measure the  $K^+$  scattered at  $0.8 < \cos \theta_{K^+} < 1.0$ . They reported  $\pi^+\Sigma^-$  and  $\pi^-\Sigma^+$  and observed a difference between the two spectra. This fact implies the existence of an interference term between  $I = 0$  and  $I = 1$ , suggesting that  $\Lambda(1405)$  is a dynamically generated state.

The CLAS Collaboration reported highly-statistical photoproduction of  $\Lambda(1405)$ . The spectra of  $\pi^-\Sigma^+$ ,  $\pi^0\Sigma^0$ , and  $\pi^-\Sigma^+$  are measured for total energies  $2.55 < W < 2.85\text{GeV}$  and  $K^+$  scattering angles of  $0.6 < \cos \theta_{K^+} < 0.9$  in the center-of-mass frame [31,32]. T. Nakamura et al. reproduced those spectra finely well using the chiral unitary model, although the reaction mechanism is not simple [25]. L. Roca et al. constructed a model with two poles using photonuclear reactions with a potential with free parameters based on the chiral unitary model [24]. They deduced a high pole is located above  $1405\text{ MeV}/c^2$ , albeit with many parameters.

HADES Collaboration reported the spectra of  $\Lambda(1405) \rightarrow \pi^\mp\Sigma^\pm$  using the  $pp \rightarrow K^+\Lambda(1405)$  reaction with a  $1405\text{GeV}/c$   $p$  beam. The peak position of the spectra was located below  $1400\text{GeV}/c$ . M. Hassanvand et al. obtained the mass and width of  $\Lambda(1405)$  with  $M = 1405.1^{+11}_{-9}\text{MeV}/c^2$  and  $\Gamma = 62 \pm 10\text{MeV}/c^2$  by adapting phenomenological analysis. On the other hand, J. Siebenron et al. argue that the data can be reproduced in a two pole structure such as the chiral unitary model.

### 1.3 $\bar{K}N$ interaction and $\Lambda(1405)$

As mentioned before,  $\Lambda(1405)$  is closely related to the  $\bar{K}N$  interaction. One way to measure the  $\bar{K}N$  interaction on the  $\bar{K}N$  threshold is to measure X-rays from Kaonic hydrogen. In this method, the  $\bar{K}N$  interaction is determined by measuring the shift of the X-ray emitted from the Kaonic hydrogen from the electromagnetic interaction. The results of this measurement were previously thought to be repulsive, but the E228 experiment performed at KEK-PS by Iwasaki et al. concluded that the interaction is attractive [12].

Then, the SIDDHARTA collaboration performed experiments with higher precision [14]. The results of this experiment were used as a constraint for analyzing  $\bar{K}N$  scattering, and the pole position of  $\Lambda(1405)$  was deduced by several theorists [16].

### 1.4 $d(K^-, n)$ reaction

As described before situation, direct measurement of  $\bar{K}N \rightarrow \pi\Sigma$  scattering is desired. But the reaction can not happen in free space due to energy conservation. For the reason, we performed the J-PARC E31 experiment [13], which measure  $d(K^-, N)\pi\Sigma$  at  $\theta_N = 0^\circ$  with  $1\text{GeV}/c$   $K^-$  beam. Fig[1.1] shows diagrams about 1-step and 2-step reactions in left and right figures. Because the total energy of  $K^-$  beam and one nucleon is about

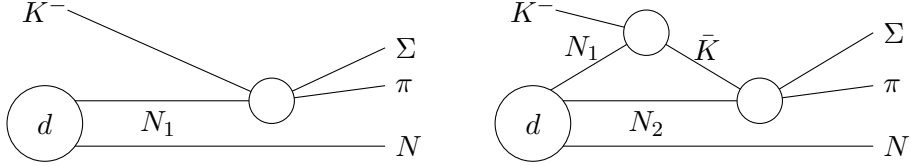


Figure 1.1: Feynman diagrams about  $d(K^-, N)\pi\Sigma$  reaction. The left and right figures indicate about 1-step and 2-step reactions, respectively.

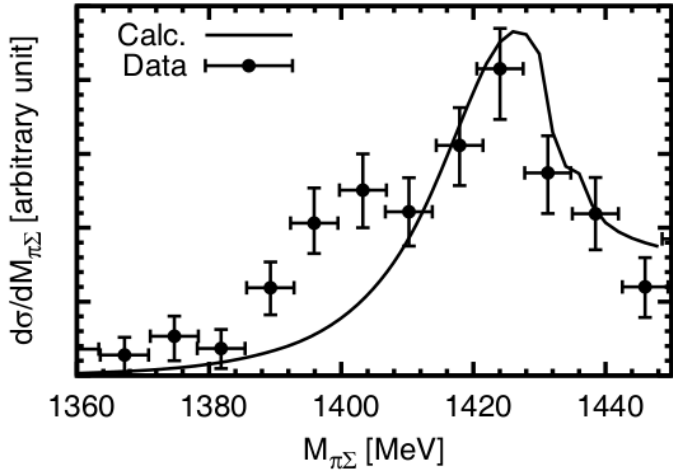


Figure 1.2: This figure shows  $\pi^+\Sigma^-$  spectra of  $K^- + d \rightarrow \pi^+ + \Sigma^- + n$  with 800 MeV incident  $K^-$  momentum calculated by the chiral unitary model [38] (solid line) and experimental data measured by the bubble chamber [37] (error bar).

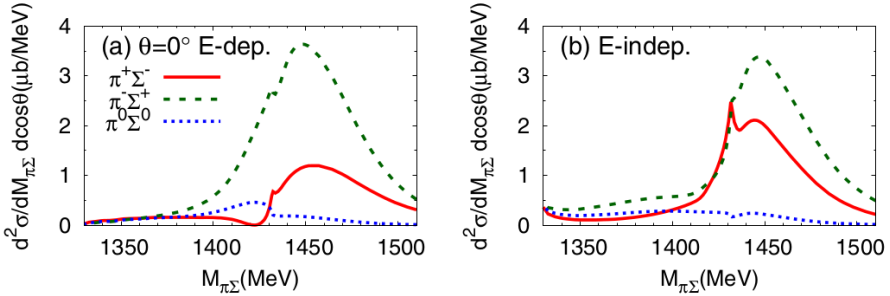


Figure 1.3:  $K^- d \rightarrow n\pi\Sigma$  calculated spectra using AGS equation by Ohnishi et al. [43]. Left and right figures indicate energy independent and dependent model, respectively.  $\pi^+\Sigma^-$ ,  $\pi^0\Sigma^0$  and  $\pi^-\Sigma^+$  indicate red solid line, blue dotted line and green dash line.

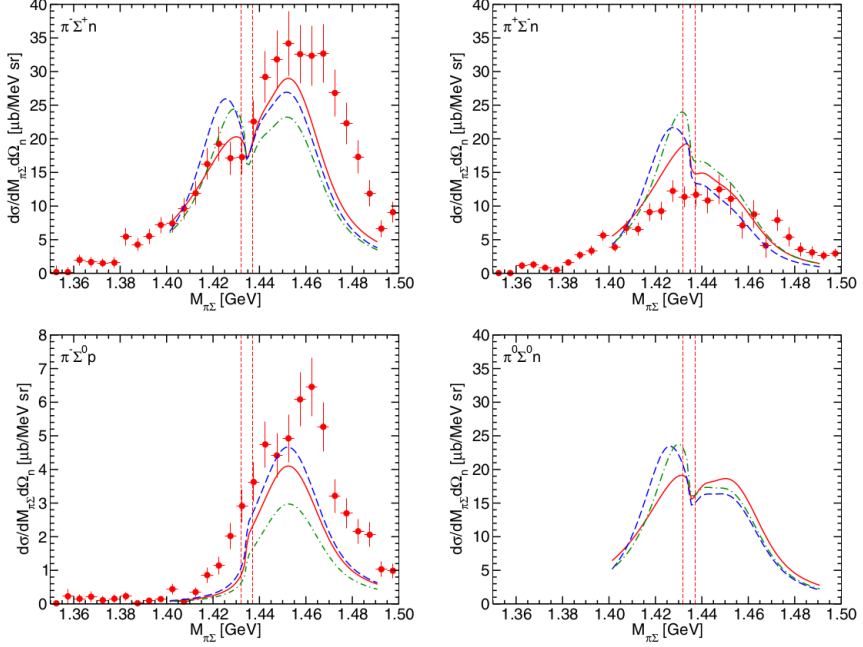


Figure 1.4: Theoretical calculation using Faddev eqation by Miyagawa et el. [39]. Left top, right top, left bottom and right bottom figures represent about  $\pi^-\Sigma^+$ ,  $\pi^+\Sigma^-$ ,  $\pi^-\Sigma^0$  and  $\pi^0\Sigma^0$  channel, respectively. The result of  $\pi^-\Sigma^+$ ,  $\pi^+\Sigma^-$  and  $\pi^-\Sigma^0$  by pilot run of J-PARC E31 experiment [40] is plotted at same figure. Red, green and blue indicates recent analysis by A. Cieplý and J. Smejkal [35], energy dependent model by Ohnishi et el. [43] and old analyssi by E. Oset, A. Ramos, and C. Bennhold [41]. Red dash vertical lines indicates  $K^0n$  (higher) and  $K^-p$  (lower) mass threshod.

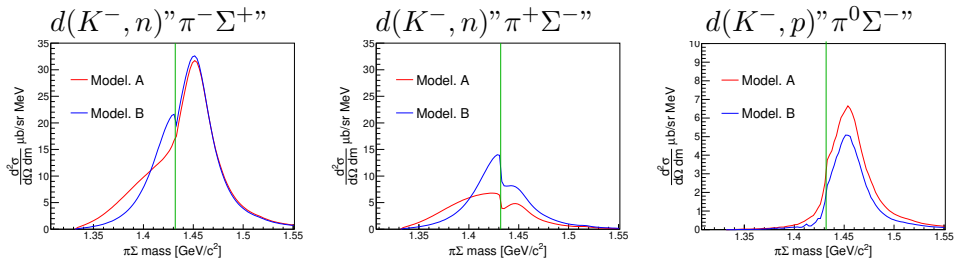


Figure 1.5: The calculated spectra by the DCC method [44]. Left, center and right figures show  $\pi^-\Sigma^+$ ,  $\pi^+\Sigma^-$  and  $\pi^0\Sigma^-$ , respectively. Red and blue lines represent model.A and B, respectively. Green vertical line indicates the  $K^-p$  mass threshold.

$2.1\text{GeV}/c^2$  and fermi momentum of deuteron is smaller than  $0.2\text{GeV}/c^2$ , 1-step reaction is negligibly small around  $\bar{K}N$  threshold in  $\pi\Sigma$  invariant mass. In 2-step reaction, induced  $K^-$  knock out a nucleon and recoiled backward. The recoiled  $\bar{K}$  react with the residual nucleon and become to  $\pi\Sigma$ . Because the recoiled momentum is small  $\sim 0.2$  GeV/ $c$  near the  $\bar{K}N$  threshold, S-wave scattering is dominant in the 2-step reaction.

Some theoretical calculation using various meson-baryon interactions and calculation methods was performed about this reaction. Fig.[1.2] shows about the chiral unitary model [38]. The bubble chamber experiment of  $K^- + d \rightarrow n + \pi^+ + \Sigma^-$  reaction with  $0.686\text{-}0.844$  GeV/ $c$   $K^-$  beam is shown in same figure [37].

Ohnishi et el. calculated by AGS equation [43]. They using 2 type meson-baryon interaction, one is phenomenological potential reproducing mass and width of PDG value and the other is effective chiral Lagrangian. Phenomenological potential is called energy independent model and the chiral Lagrangian is called energy dependent model, these shown in Fig[1.3]. The calculation using Faddev equation was performed by Miyagawa et el. [39]. They adopted partial wave analysis by KSU group [42] at 1-step  $K^-N \rightarrow \bar{K}N$  scattering, because incident K- momentum is larger than the region can be adopted to chiral analysis. They adopt some scattering parameters at 2-step scattering as shown in the Fig.[1.4]. Red solid line indicates recent analysis of KN potential by A. Cieplý and J. Smejkal [35], green dotted line indicates energy dependent model by Ohnishi et el. [43] that mention before and blue dashed line indicates analysis by E. Oset, A. Ramos, and C. Bennhold [41], performed about twenty years before.

Kamano et el. also calculated this reaction using the DCC method [44]. Although the DCC method has 2 models due to shortage of data below the  $\bar{K}N$  threshold as mentioned above, the DCC model cover wide energy region from high energy about 1-step  $K^-N \rightarrow \bar{K}N$  scattering to below the  $\bar{K}N$  threshold.

In this paper, we present obtained  $d(K^-, n)''\pi^-\Sigma^+$ ,  $d(K^-, n)''\pi^+\Sigma^-$  and  $d(K^-, p)''\pi^0\Sigma^-$  spectra by the J-PARC E31 experiment and decompose isospin. We discuss how much explained and how to improve theoretical calculation, especially the DCC method from point of isospin relation, so  $I = 0$ ,  $I = 1$  and their interference term.

## Chapter 2

# Experimental setup

### 2.1 Experimental facility

#### 2.1.1 J-PARC

Our experiment was performed at the K1.8BR beamline at hadron facility of the J-PARC located at the Tokai site in Ibaraki Prefecture [46, 47]. J-PARC, which means Japan Proton Accelerator Research Complex, consists of some facilities, which are nuclear transmutation facility, materials, and life experimental facility, muon facility, neutrino facility, and hadron facility. The concept of the J-PARC is to provide various secondary beam for the above purpose. The J-PARC has three accelerators, first one is linac which is injector and accelerates proton beam to  $400\text{MeV}/c$ , second is RCS (Rapid Cycling Synchrotrons) which accelerates proton beam to  $3\text{GeV}$ , which was provided to materials and life experimental facility and muon facility. Next is MR (Main Ring) which accelerates proton beam to  $30\text{GeV}/c$ , which beam was extracted by two methods. One is the fast extraction (FX) for the neutrino facility to produce a neutrino beam which transported to the super Kamiokande. The other is the slow extraction (SX) for the hadron facility. In this extraction, bunched beam in the MR is gradually extracted as scraping. For this purpose, the  $30\text{GeV}/c$  proton beam was extracted about 2-second with a 5.2-second repetition cycle.

This continuous beam is irradiated on the primary target that is  $6\text{mm} \times 6\text{mm} \times 66\text{mm}$  golden block to generate secondary beam which includes anti-proton, pion, kaon and so on that is not naturally exist. The secondary beam was transported to several beamlines.

The present experiment was performed at the K1.8BR beamline, which was placed at north of the hadron facility and branched from the K1.8 beamline which was optimized for beam whose momentum is around  $1.8\text{GeV}/c$ .

### 2.1.2 K1.8BR beam line

The K1.8BR beamline was planned to use low momentum kaon beam whose upper limit is  $1.2 \text{ GeV}/c$ . Such kaon decays with short decay time, so beam line length should be short. So, our beamline length was designed at about 31m by branching the K1.8 beamline. Fig 2.1 shows a schematic view of the K1.8BR beamline.

The D1 magnet accumulates secondary particles with the 6-degree aperture and the D2 magnet selects a specific momentum beam with  $\pm 3\%$  momentum bite. Intermediate focus slit (IF Slit) defined beam profile to increase the number of kaon beam while keeping good kaon and another particle ratio. Kaon and other particles were separated by the electrostatic separator (ES1) using vertical direction statical electronic field which uses the principle that different mass charged particles pass different trajectories by the electrical field. The kaon beam was kicked up by the CM1 magnet, was bent in the opposite direction by ES1 and was kicked to parallel direction by the CM2 magnet. Other particles pass through different position of vertical direction at mass slit1 (MS1), so these were intercepted by the MS1. Also, the horizontal directional slit of the MS1 defines the dispersive of the beam. The D3 magnet switched beam to the K1.8 or the K1.8BR. After the D3 magnet, an SQDQD system is employed to focus the beam on the experimental target at FF of the K1.8BR beam line. The first-order beam envelope calculated by the TRANSPORT code [48] is shown in Fig 2.2.

The data for the  $d(K^-, p)$  has been taken in May-June in 2016 which is so-called as MR-RUN69 and the data for the  $d(K^-, n)$  has been taken in Jan-Feb in 2018 which is so-called as MR-RUN78.

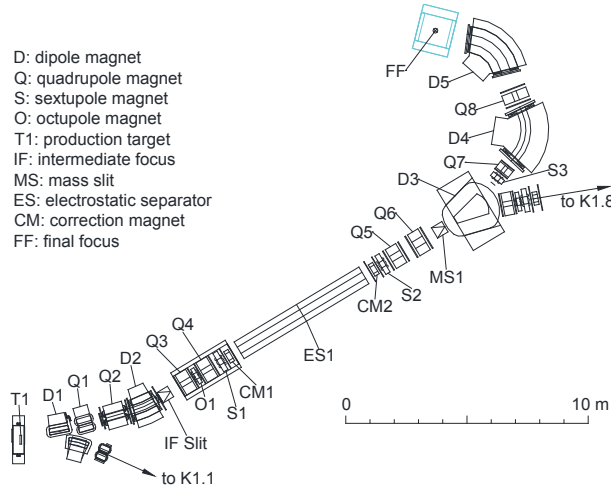


Figure 2.1: Schematic view of the K1.8BR beam line.

Table 2.1: Parameters of the beam-line magnets. D5 field is a typical monitored value. Other field values are interpolations of measured points.

Element	J-PARC designation	Gap or bore/2 (cm)	Effective length (cm)	Bend (deg)	Current (A)	Field at pole (kG)
D1	5C216SMIC	8	90.05	10	-369	-6.7444
Q1	NQ312MIC	8	67.84		-357	-3.075
Q2	Q416MIC	10	87.04		-668	3.872
D2	8D218SMIC	15	99.65	15	-698	-8.7673
IF-H	Movable horizontal slit for acceptance control					
IF-V	Movable vertical slit, $(y \phi)=0$					
Q3	Q410	10	54.72		-679	-4.108
O1	O503	12.5	15		-15	-0.29
Q4	Q410	10	54.72		-776	4.692
S1	SX504	12.5	27.6		-42	-0.29
CM1	4D604V	10	20	(0.856)	348	1.633
ES1	Separator	10	600		E=-500 kV/10 cm	
CM2	4D604V	10	20	(0.856)	348	1.630
S2	SX504	12.5	27.6		-136	1.02
Q5	NQ510	12.5	56		-498	4.218
Q6	NQ610	15	57.2		-535	-4.316
MOM	Movable horizontal slit for momentum acceptance control					
MS1	Movable vertical slit for $K-\pi$ separation $(y \phi)=0$ , $(y y)=0.844$ , $(y \theta\phi)=(y \phi\delta)=0$					
D3	6D330S	15	165.1	20	210	-7.064
S3	SX404	10	20		-34	-1.062
Q7	Q306	7.5	30.34		-464	4.026
D4	8D440S	20	198.9	60	-1938	-17.906
Q8	NQ408	10	46.5		-110	0.671
D5	8D240S	20	195.9	55	-1666	-16.437

Primary beam momentum	30 GeV/c proton
Primary beam power	50kW
Proton per spill	$4.8 \times 10^{13}$
Repetition cycle	5.2 sec
Spill Length	2 sec
Spill duty factor	50%
Spill extraction efficiency	99.5 %
Production target	Au(50 % loss)
Production angle	6 degrees
Length (T1-FF)	31.3 m
Momentum range	1.2 GeV/c max.
Acceptance	2.0 msr.% ( $\Delta\Omega \cdot \Delta p/p$ )
Momentum bite	$\pm 3 \%$

Table 2.2: Parameters of the K1.8BR beamline and typical operation condition

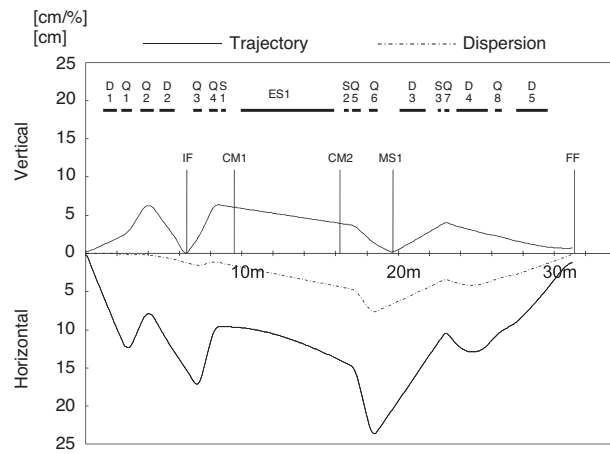


Figure 2.2: First-order beam envelope calculated by the TRANSPORT.

## 2.2 Beam line detectors

### 2.2.1 Overview

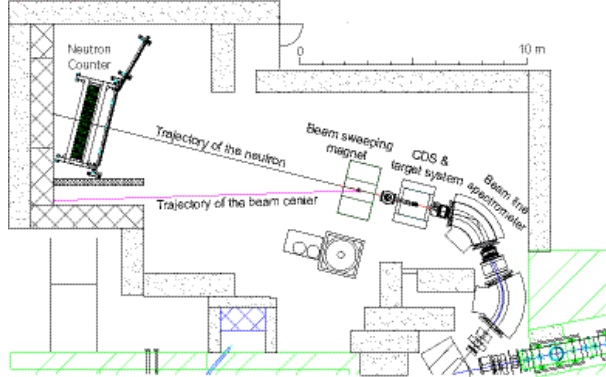


Figure 2.3: Schematic view of the experimental hall at the K1.8BR.

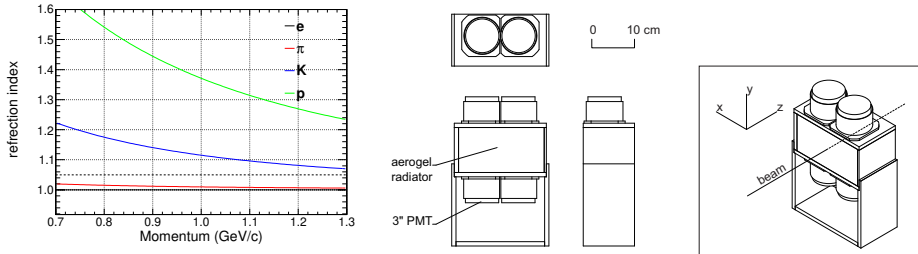


Figure 2.4: The right figure shows a schematic drawing of the AC. The left figure represents the threshold of reflection index for Cherenkov radiation and the momentum. The horizontal dotted line shows the reflection index of the Aerogel ( $n=1.05$ ).

A kaon was identified by threshold type of aerogel Cherenkov counter (AC) with refractive index  $n = 1.05$  which can identify kaon and pion around  $0.7 \sim 1.2 \text{ GeV}/c$  as Fig2.4. This offline level identification information was used for beam line tuning, especially koan and another particle separation. We first search ES1 voltage and CM1/2 current which maximize kaon yield. After that, IF slit and MS1 slit were adjusted to maximize the number of kaons while keeping an acceptable level of pion contamination. In this tuning, vertical direction opening width was decided to avoid pion peak come from direct production at the T1 target and horizontal direction was set to reject pion come from magnets and so on installed in beamline which so-call pion halo.

The beam particle identification was also performed using the TOF

method by beamline hodoscope counter (BHD) and time-zero (T0) counter which has about  $7.7\text{m}$  flight length. The T0 counter was installed at downstream of D5 magnet and was rotated by 45 degrees about the beam direction axis, which consists of 5 segmented plastic scintillation counters whose size is  $160\text{mm}$  (height)  $\times$   $32\text{mm}$  (width)  $\times$   $10\text{mm}$  (thickness), so the T0 counter covers  $160\text{mm} \times 160\text{mm}$  effective area. A counter uses the Saint-Gobain BC420 scintillator and attached readout which is  $3/4$  inch Hamamatsu H6612B photomultipliers to both sides of the scintillator.

The BHD counter was installed at just upstream of the D4 magnet, which consists of 20 segment plastic scintillaton counters whose size is  $160\text{mm}$  (height)  $\times$   $20\text{mm}$  (width)  $\times$   $5\text{mm}$  (thickness), so the BHD counter covers  $400\text{mm}$  (horizontal)  $\times$   $160\text{mm}$  (vertical) effective area. A counter uses the same photomultipliers as the T0 counter. Since beam rate was a few M events per spill, photomultipliers were attached high voltage booster to the last three dynodes to avoid gain drop due to high current by high rate beam.

### 2.2.2 Beam momentum analyzer

Beam momentum was reconstructed from the second-order transfer matrix of the D5 magnet, whose magnetic field was monitored during the experiment with high-precision Hall probe Lakeshore 475 which has  $\sim 10^{-5}\text{ T}$  resolution. The fluctuation of the magnetic field was  $\sim 2 \times 10^{-4}$  that correspond to  $0.2\text{GeV}/c$  for  $1\text{GeV}/c$  beam. Also, helium bag was install at pass way of the D5 magnet to suppress the multiple scattering effect due to materials.

For measuring tracks of upstream and downstream of the D5 magnet, planer type drift chambers were installed at these positions. These chambers were named the BLC1 and the BLC2 which has two components, BLC1a/b and BLC2a/b, respectively. These chamber sets were rotated 45 degrees about the beam direction axis. All components have the  $UU'VV'UU'VV'$  configuration and 32 sense wires pre layer, so each component has 256 readout channels. Drift lengths of the BLC1 and the BLC2 are 4mm and 2.5mm which corresponds to cover  $252\text{mm} \times 252\text{mm}$  and  $157.5\text{mm} \times 157.5\text{mm}$  area, respectively. These drift chambers use  $12.5\text{ }\mu\text{m}$  diameter gold-plated tungsten wires with 3% rhenium for sense wires and  $75\text{ }\mu\text{m}$  diameter copper-beryllium wires for potential wires. The cathode planes made of  $12.5\text{ }\mu\text{m}$  aluminized Kapton. The spatial resolution was evaluated at about  $200\text{ }\mu\text{m}$  which was estimated at  $10^{-3}$  corresponding to  $1\text{GeV}/c$  for  $0.1\text{GeV}/c$  beam. These drift chambers use isobutane and argon including methylal (dimethoxy-methane) to pass through its bubbler whose temperature is  $4^\circ\text{C}$  in the refrigerator mixed to 1:4 by the mass-flow controller. As a result, the ratio of isobutane, argon and methylal was 20%, 76% and 4%.

### 2.2.3 BPD

BPD which means backward proton detector was developed for the measurement of backward proton decay from  $\Lambda$  in  $Y^* \rightarrow \pi^0 \Sigma^0 \rightarrow \pi^0 \gamma \pi^0 \Lambda$  decay scheme which was installed at most upstream of the CDS. The scattered angle of  $Y^*$  is enhanced backward scattering, especially below the threshold due to small momentum transfer. The BPD was installed to obtain large acceptance for these protons. The BPD is a plastic scintillator hodoscope array with a size of 350mm (horizontal)  $\times$  340mm (vertical). It is segmented into 70 units of 5mm  $\times$  5mm  $\times$  340mm scintillation counter made of Eljen EJ-230. Two MPPCs with a 3mm  $\times$  3mm sensitive area (Hamamatsu S10362-33-050C) were directly put on both sides of each slab. The present thesis explains the  $\pi^\pm \Sigma^\pm$  and the  $d(K^-, p)'' \pi^- \Sigma^0$  modes analysis, so BPD was used only energy loss calculation.

### 2.2.4 Vertex chamber - BPC

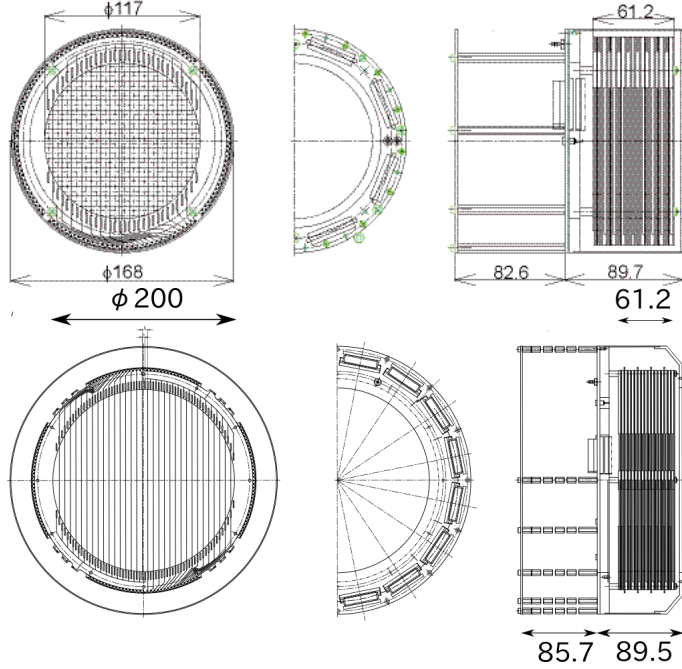


Figure 2.5: Schematic view of the BPC. Above figure shows about MR-RUN69. Bottom figure shows about MR-RUN78.

BPC which means backward proton chamber was developed for the measurement of backward proton decayed from hyperons that come from  $\pi^0 \Sigma^0$  mode. The BPC also used beam tracking at just upstream of the experimental target for the definition of reaction vertex point. The BPC was installed at just upstream of the experimental target where is in the CDS

described after. The BPC is a planer type drift chamber which has a circular plane to maximize effective area in limited space. The BPC configuration is XX'YY'XX'YY', so the BPC has 8 layers.

In MR RUN69, the chamber with 168mm diameter outer which has 15 sense wires per layer with 3.6mm drift length corresponding to 111.6mm effective area was used as the BPC. In this run, the inner hodoscope (IH) was installed in CDS for the trigger counter to evaluate CDC efficiency.

In MR RUN78, the IH was removed to maximize acceptance of backward proton so larger chamber was used as the BPC whose outer size is 290mm diameter and 32 sense wires per layer with 3.0mm drift length corresponding to 189mm effective area.

These chambers were used  $50\mu\text{m}$  diameter copper-beryllium wire for potential wires and  $12.5\mu\text{m}$  diameter gold-plated tungsten. These cathode planes are made of  $9\mu\text{m}$  carbon aramid foil. These are 120 read-outs and 256 read-outs in MR-RUN69 and MR-RUN78, respectively.

### 2.2.5 Beam definition counter

The beam definition counter (DEF) was installed just upstream of the target the vacuum chamber for the definition of the beam to avoid particle not hitting the liquid deuterium target. In our beamline, a half of kaon hits the experimental targets due to large beam size. High trigger rate not only is the cause of low data quality but also the cause of decreasing DAQ efficiency due to computer busy, so the DEF signal was coincided with beam trigger made by the T0 and BHD and was used reducing beam trigger rate. The trigger rate was successfully suppressed by about 30% by this counter.

## 2.3 Target system

### 2.3.1 Liquid $D_2$ target system

A side view of the cryostat for the liquid  $D_2$  target is shown in Fig2.6. Deuterium was stored 1000l in a tank as gases which is room temperature and 2 atm keeping positive pressure after liquefaction for avoiding contamination from other materials. The  $D_2$  gas is fed into the cryostat through the top flange. Cooling of  $D_2$  was performed by the Gifford–McMahon (G–M) refrigerator (Sumitomo Heavy Industries, Ltd., RDK-145D and CSA-71A) built into the cryostat. The cooling was performed by 2-step. The cooling power at the first and second stages is 35W at 50K and 1.5W at 4.2K, respectively. A copper plate was anchored to the first-stage cold head of the G–M refrigerator in inlet pip for the pre-cooling of the  $D_2$ . Another inlet pipe was directly connected through the top flange to the head exchanger for measuring the pressure of the  $D_2$  target inside of the heat exchanger. Since this pipe has a larger conductance, a safety valve that prevents a

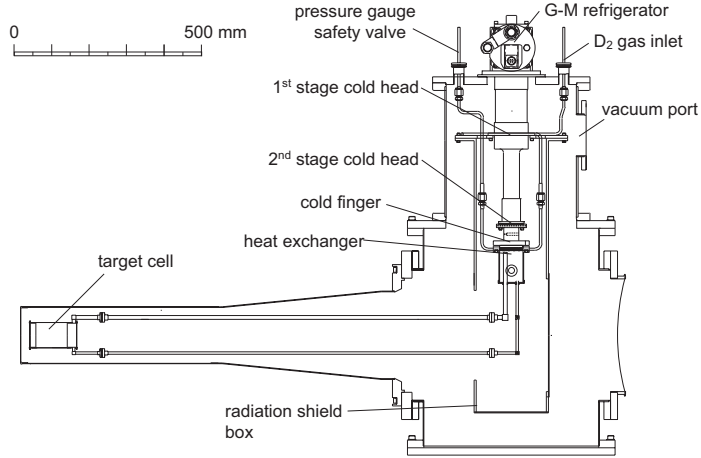


Figure 2.6: Schematic drawing of the liquid  $D_2$  cryostat.

sudden pressure rise is also connected to it. The  $D_2$  gas is cooled in the heat exchanger where the second stage of the G–M refrigerator is thermally contacted.

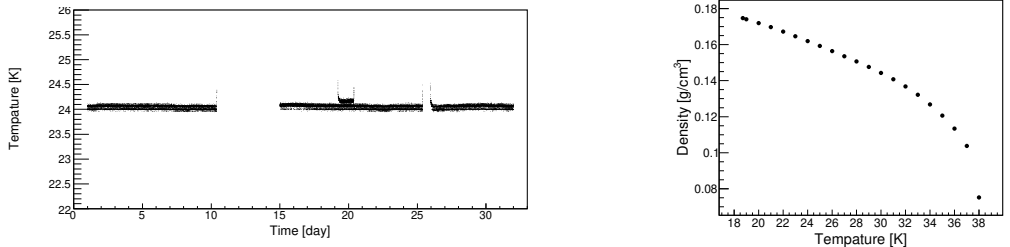


Figure 2.7: The left figure shows the temperature of the  $D_2$  target. The right figure shows the relation of the density and the  $D_2$  temperature at 1 atm.

The target cell was 6.8cm diameter and 12.5cm length cylinder made of PET. Liquifregrated  $D_2$  was transferred by downpipe and warmed liquid  $D_2$  by the heat load was returned through the upper pipe, so the heat was effectively transferred between the target cell and the heat exchanger [51]. Since the temperature range of liquid  $D_2$  is narrow as 18.7-23.8K at 1 atm, the temperature of the  $D_2$  should be controlled in the liquid range to avoid blocking due to the solid  $D_2$ . Since the cooling power of the second stage of the G–M refrigerator is larger than the heat load on the low-temperature parts, we have installed a heater near the cold finger to compensate for the heat load. The current in the heater is controlled by a proportional-

integral-derivative (PID) algorithm with an input of the temperature of the heat exchanger. Target cell temperature in MR-RUN78 was represented in Fig2.7 which was monitored by Pt-Co thermometer (CHINO R800-6) whose tolerance was  $\pm 0.5\text{K}$ . The same figure also shows the relation of temperature and density of  $D_2$  at 1 bar. The error of  $D_2$  density was estimated at  $1.5 \times 10^{-3}[\text{g}/\text{cm}^3]$  from tolerance and fluctuation.

## 2.4 The cylindrical detector system

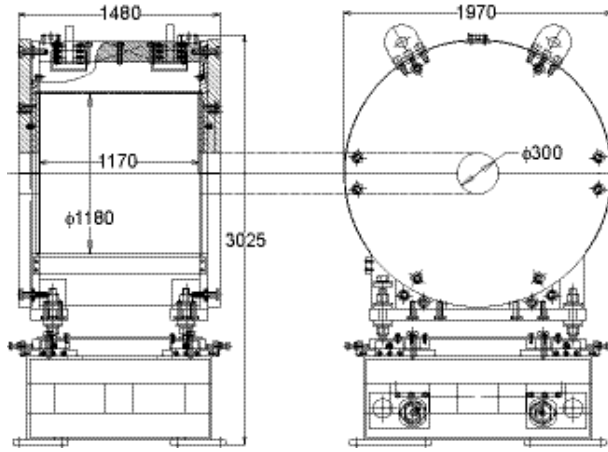


Figure 2.8: Design of the solenoid magnet (all dimensions in mm)

The cylindrical detector system (CDS) surrounds the experimental target system to measure produced charged particles. The CDS consists of three parts, the outermost part is the solenoid magnet to make the uniform magnetic field for momentum analysis, next is the cylindrical detector hodoscope (CDH) to measure time-of-flight from the T0 and make trigger signal, and the cylindrical drift chamber (CDC) to measure the trajectory in the magnetic field, by which the momentum of a charged particle was analyzed. Particle identification was performed by the momentum and T0-CDH TOF.

### 2.4.1 Solenoid magnet

The CDS is a solenoid type spectrometer whose bore diameter is 1.18m and the length is 1.17m with an overall weight is about 23 tons. The design of the solenoid magnet is shown in Fig2.8. The magnet provides a uniform field strength inside the tracking volume ( $|z| < 420\text{mm}$ ). In the present experiment, it is operated at 0.7T.

### 2.4.2 Cylindrical drift chamber

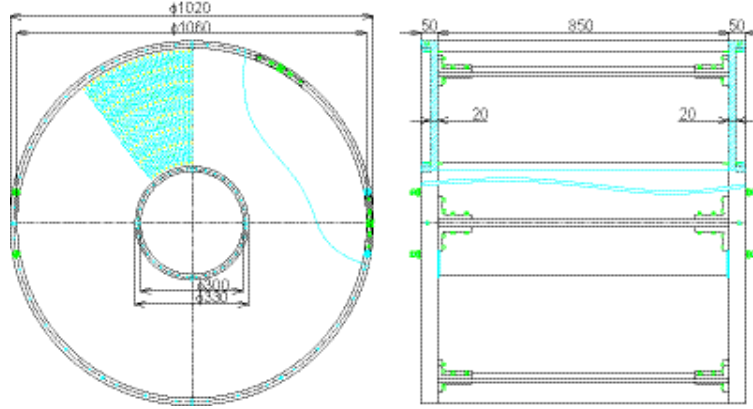


Figure 2.9: Design of the CDC (all dimensions in mm). The CDC consists of two aluminum end-plates, a 1mm thick CFRP cylinder as an inner wall, and six aluminum posts that are placed outside the tracking volume.

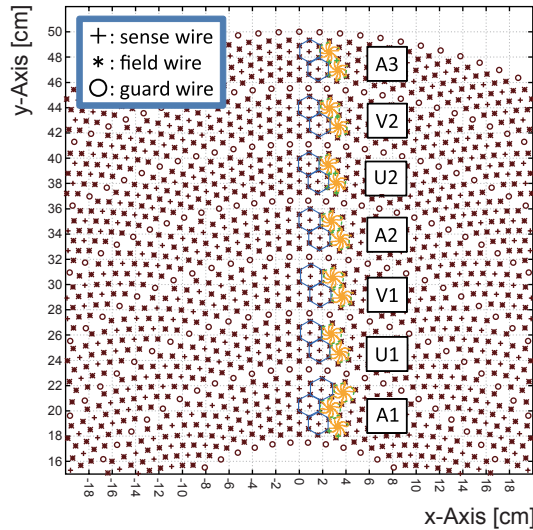


Figure 2.10: Cell structure of the CDC.

The CDC is a cylindrical wire drift chamber that contains 15 layers of anode wires. The structure of the CDC is shown in Fig 2.9. The outer radius is 530mm and the inner radius is 150mm, with a total length of 950mm. The wire length of axial layers is 833.8mm, thus the angular coverage is  $49^\circ < \theta < 131^\circ$  in the polar angle region corresponding to a solid angle coverage of 66% of  $4\pi$ . The CDC consists of two aluminum end-plates of 20mm thickness, a 1mm thick CFRP cylinder as the inner wall of the CDC,

Table 2.3: Wire configuration of the CDC.

super layer	layer	wire direction	radius (mm)	cell width (degree)	cell width (mm)	stereo angle (degree)	signal channels per layer
A1	1	X	190.5		16.7	0	
	2	X'	204.0	5.00	17.8	0	72
	3	X	217.5		19.0	0	
U1	4	U	248.5		17.3	-3.55	
	5	U'	262.0	4.00	18.3	-3.74	90
V1	6	V	293.0		18.4	3.77	
	7	V'	306.5	3.60	19.3	3.94	100
A2	8	X	337.5		17.7	0	
	9	X'	351.0	3.00	18.4	0	120
U2	10	U	382.0		16.0	-3.28	
	11	U'	395.5	2.40	16.6	-3.39	150
V2	12	V	426.5		16.7	3.43	
	13	V'	440.0	2.25	17.3	3.54	160
A3	14	X	471.0		16.4	0	
	15	X'	484.5	2.00	16.9	0	180

and six aluminum posts that are placed outside the tracking volume. The CDC uses gold-plated tungsten of  $30\mu\text{m}$   $\phi$  for the sense wires, and gold-plated aluminum of  $100\mu\text{m}$   $\phi$  for the field and guard wires. These wires are supported by feedthroughs with a bushing inserted at the end. Bushes with an  $80$  and  $200\mu\text{m}$   $\phi$  hole are used for the sense and field/guard wires, respectively.

The CDC has 15 layers of small hexagonal cells with a typical drift length of 9mm, which are grouped int 7 super layers as shown in Fig2.10. Table 2.3 gives the detailed parameter of the wire configuration. The layers are in the radial region from 190.5mm (layer 1) to 484.5mm (layer 15). The 8 stereo layers tilted by about  $3.5^\circ$  are used to obtain longitudinal position information. The number of readout channels is 1816 and the total number of wires in the CDC is 8064.

The drift gas is 1 atm of mixed argon (50%)-ethane (50%). A high voltage is applied to the field and guard wires, and the sense wires are kept at ground potential. For the first super-layer (A1) and the second one (U1), a high voltage of -2.8kV is applied to the potential wires, and -2.7kV to the potential wires of the other super-layers. Also, -1.5kV, -1.8kV, and -0.6kV are applied to the innermost, the outermost, and the other guard wires, respectively.

### 2.4.3 Cylindrical detector hodoscope

The CDH is a segmented plastic scintillation counter used for the charged particle trigger and particle identification. The CDH is located at a radius

of 544mm from the beam axis covering a polar angle range from 54 to 126 degree corresponding to a solid angle coverage of 59% of  $4\pi$ .

The CDH consists of 36 modules, individually mounted on the inner wall of the solenoid magnet. The scintillators are made of ELJEN EJ-200, with dimensions of 790mm in length, 99mm in width, and 30mm in thickness. The scintillation light is transferred through light guides to a pair of Hamamatsu R7761 fine-mesh 19-dynode photomultipliers 1.5 inches in diameter.

The CDH is operated in the 0.7T magnetic field with a typical PMT gain of  $\sim 10^6$ . The measured average time resolution of the CDH without a magnetic field is  $71 \pm 3$  ps ( $\sigma$ ), obtained with cosmic ray data. The error represents the variation among the segments.

#### 2.4.4 Inner hodoscope

An inner hodoscope (IH) is a segmented plastic scintillation counter mounted on the inner wall of the CFRP cylinder of the CDC at a radius of 140mm from the beam axis. The IH consists of 24 ELJEN EJ-200 scintillators with a dimension of 600mm in length, 27mm in width, and 3mm in thickness. Each segment is overlapped by 1mm due to the strong magnetic field and limited space, multi-pixel photon counters (MPPCs) with a 3mm  $\times$  3mm sensitive area were used (Hamamatsu S10362-33-100C). The scintillation light is collected by 4 wavelength-shifting fibers embedded in the scintillator and connected to an MPPC with a specially designed connector. The MPPC signal is read out by using a preamplifier.

The IH was used as a trigger counter for the efficiency estimation of the CDC. The IH was removed in MR RUN78 to increase acceptance for the backward scattered proton.

### 2.5 Forward detector systems

Beam pass through the target was swept to the beam dump direction by the beam sweep magnet called Ushiwaka, which also used to sweep positive charged particles to the opposite direction of the beam.

The neutron counter array (NC) was placed at about 15m downstream of the target to detect neutral particles and measure its velocity by TOF method. The charged particle was rejected by the beam veto counter (BVC) and the charged veto counter (CVC), which was installed at just upstream of the Ushiwaka and the NC, respectively. The proton counter was located at the opposite position of the beam dump to measure positive charged particles. Half of the CVC was also used for a positive charged particle. Because the trajectory of the charged particle depends on its momentum, the forward drift chamber was installed at upstream of the Ushiwaka magnet to decide its trajectory. The momentum of forward positive charged particle was evaluated by the TOF method.

### 2.5.1 Beam sweeping magnet

The Ushiwaka placed at 250cm downstream of the target has a large aperture which of 82cm (horizontal)  $\times$  40cm (vertical) and a pole length of 70cm, which is larger than the acceptance of the NC. The Ushiwaka can be applied to 1.6T at maximum value.

### 2.5.2 Beam veto counter

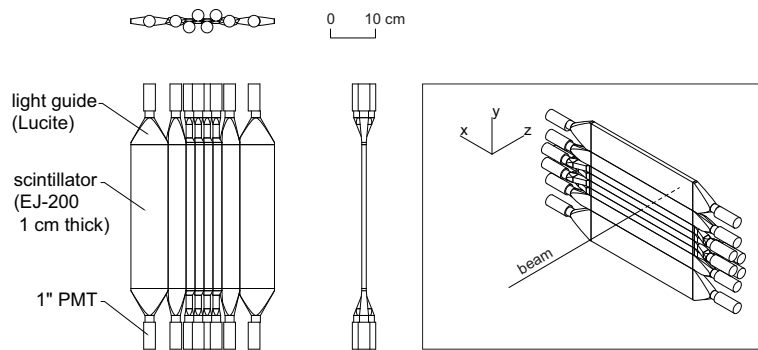


Figure 2.11: Schematic view of the BVC.

The BVC was attached on the downstream flange of the target cryostat to reject charged particle contamination to neutral trigger, especially come from beam particle pass through. The coverage size of the BVC is 320mm (height)  $\times$  320mm (width)  $\times$  10mm (thickness) made of ELJEN EJ-200. This size is large enough to cover the acceptance of the neutron counter. The BVC is horizontally segmented int 8units with different sizes as shown in Fig2.11 to avoid the over-concentration to the beam on the central segments. In this position, there is some leak magnetic field from the solenoid magent of the CDS and the Ushiwaka magnet so its read-out used 1-inch fine-mesh Hamamatsu R5505 photomultipliers which were attached on both ends of each scintillator segment through Lucite light guides.

### 2.5.3 Neutron counter array

The neutron counter array was placed at 14.7m downstream of the target to measure neutron comes from  $d(K^-, n)$  reaction. The NC consist of 7 layers and each layer has 16 segmented plastic scintillator whose size is 20cm (width)  $\times$  150cm (height)  $\times$  5cm (thickness). The NC is covered 6.2° in horizontal and 2.9° in vertical. The scintillators for the first 3 layers are made of Saint-Gobain BC408 and the other four layers are made of Saint-Gobain BC412. 2 inch Hamamatsu H6410 photomultipliers were attached to both sides of the scintillator through a Lucite light guide. The average time resolution of the neutron counter, measured with cosmic rays, is  $92 \pm 10$  ps

$(\sigma)$ . The error represents variation among the segments. Detection efficiency about  $1.0\text{GeV}/c$  neutron was estimated by  $K^- p \rightarrow K^0 n$  reaction using  $H_2$  target which is described Sec.3.5.2

#### 2.5.4 Charge veto counter

The charged veto counter (CVC) was placed at just upstream of the NC for the rejection of charged particles in the NC. The CVC consists of 34 segmented plastic scintillators whose size is 10cm (width)  $\times$  150cm (height)  $\times$  5cm (thickness). The scintillator was attached 2 inch Hamamatsu H6410 photomultipliers through the Lucite light guide. The scintillator is of Eljen EJ-200 type. The average time resolution measured with cosmic rays is  $78 \pm 7$  ps  $(\sigma)$ . The error represents the variation among the segments. Half of the CVC counter was used for the forward proton measurement.

#### 2.5.5 Proton counter

The proton counter (PC) was placed at opposite side of beam sweeping direction to measure inflight- $(K^-, p)$  reaction. The PC consists of 27 segmented plastic scintillators whose size is the same as the CVC. The PC has 2.7m (horizontal) and 1.5m (vertical) effective area. The scintillators made of Saint-Gobian BC408. The Hamamatsu H6410 was attached both side of scintillator through the Lucite light guide.

#### 2.5.6 Forward drift chamber

The forward drift chamber (FDC1) was attached to the Ushiwaka magnet to measure the trajectory of the forward proton before sweeping for the decision of flight-length. The FDC1 is a planer type drift chamber that has 6 layers consisting of UU'-XX'-VV'. UU' and VV' layers were tilted  $\pm 30^\circ$  about the beam axis. Each layer has a 6mm gap in each sense wires and each pair plane was located at 20mm.

### 2.6 Data acquisition system

#### 2.6.1 Overall system

In this section, the data accumulated system is explained. This experiment mainly used hodoscopes and drift chambers. Hodoscope output split into two signals. A signal direct send to the ADC (Analog-Digital-Converter). Another signal was discriminated against with some thresholds and send to the TDC(Time-Digital-Converter) that was also used as a trigger signal. Up and down readout of hodoscopes which has double readout was made coincided signal to make trigger signal.

Table 2.4: Summary of the beam-line chamber parameters.

	BLC1a	BLC1b	BLC2a	BLC2b
number of planes	8	8	8	8
plane configuration	UU'VV'UU'VV'	UU'VV'UU'VV'	UU'VV'UU'VV'	VV'UU'VV'UU'
number of sense wires in a plane	32	32	32	32
wire spacing (mm)	4	4	2.5	2.5
effective area (mm)	$256 \times 256$	$256 \times 256$	$160 \times 160$	$160 \times 160$
Sense wire material diameter ( $\mu m$ )		Au-plated W (3% Re) 12		
Potential wire material diameter ( $\mu m$ )			Au-plated Cu-Be 75	
Cathode plane material thickness ( $\mu m$ )			alminized-Kapton 12.5	
operation voltage				
potential	-1.25	-1.25	-1.25	-1.25
cathord	-1.25	-1.25	-1.25	-1.25
	BPC(Run68)	BPC(Run78)	FDC1	
number of planes	8	8	6	
plane configuration	XX'YY'X'XY'Y	XX'YY'X'XY'Y	UU'XX'VV'	
number of sense wires in a plane	15	32	64	
wire spacing (mm)	3.6	3	3	
effective area (mm)	$111.6\phi$	$189\phi$		
Sense wire material diameter ( $\mu m$ )		Au-plated W (3% Re) 12	12	
Potential wire material diameter ( $\mu m$ )		Au-plated Cu-Be 75	Au-plated Cu-Be 75	
Cathode plane material thickness ( $\mu m$ )		Cu aramid 9	alminaized-Kapton 7.5	
operation voltage				
potential	-1.50	-1.45	-1.45	
cathord	-1.50	-1.45	-1.45	

The drift chamber signal was digitized by ASD on the spot and sent to the repeater as the LDVS signal. The signal was converted to an ECL signal by the repeater and sent to the Dr.T module in the counting house.

These trigger signals were combined to make various conditions for data taking. Data taking scheme was consist of TKO creates [49] which has ADC and TDC modules to accumulate digital data which were controlled by VME-SMPs (supper memory partner) via a TKO SCH (supper controller head [50]. This system was operated by the Linux PC.

### 2.6.2 Trigger circuit

We took some triggered data in which one is beamline level to evaluate beam status and the other is the reaction required level for the specific physics. These were two timing trigger signals, one was a fast signal which was come from the beamline and the CDS and another one was about 100ns late signal which comes from forward counters. The fast signal can be made faster trigger than data signals, although late signal can not be made such a fast trigger signal. So, fast trigger signals deciding whether to accumulate the data is so-called as 1st level decision trigger and late trigger signals deciding whether to transfer the data to the PC was so-called as 2nd level decision trigger. Trigger scheme was shown in Fig3.4.

Beam trigger was a coincidence of the BHD and the T0. Beam particle was identified whether to pion or kaon by the AC installed just downstream of the T0 that also required the DEF signal to guarantee that beam was actually irradiated on the experimental target. Beamline trigger combined as follows,

$$\begin{aligned} \text{Beam} &= \text{T0} \otimes \text{BHD} \\ \text{Kaon} &= \text{T0} \otimes \text{BHD} \otimes \text{AC} \otimes \text{DEF} \\ \text{Pion} &= \text{T0} \otimes \text{BHD} \otimes \overline{\text{AC}} \otimes \text{DEF} \end{aligned}$$

For the  $d(K^-, N)$  analysis, we made forward triggers. Forward neutral trigger was required no signal in the CVC and the PC. Forward charge trigger was defined the PC and half of the CVC which is the opposite side of beam sweeping direction. These triggers were combined kaon trigger and CDH 1hit trigger which is necessary to determine the reaction vertex position. CDH 2hit trigger was accumulated to evaluate that status for 2nd level trigger condition.

$$\begin{aligned} d(K^-, n)\text{main} &= \text{Kaon} \otimes \text{CDH1} \otimes \text{NC} \otimes \overline{\text{CVC} \cup \text{BVC}} \\ d(K^-, p)\text{main} &= \text{Kaon} \otimes \text{CDH1} \otimes \text{PC} \cup \text{CVC}_{\text{half}} \\ \text{K} \otimes \text{CDH2} &= \text{Kaon} \otimes \text{CDH2} (\text{for evaluation of BVC and CVC}) \end{aligned}$$

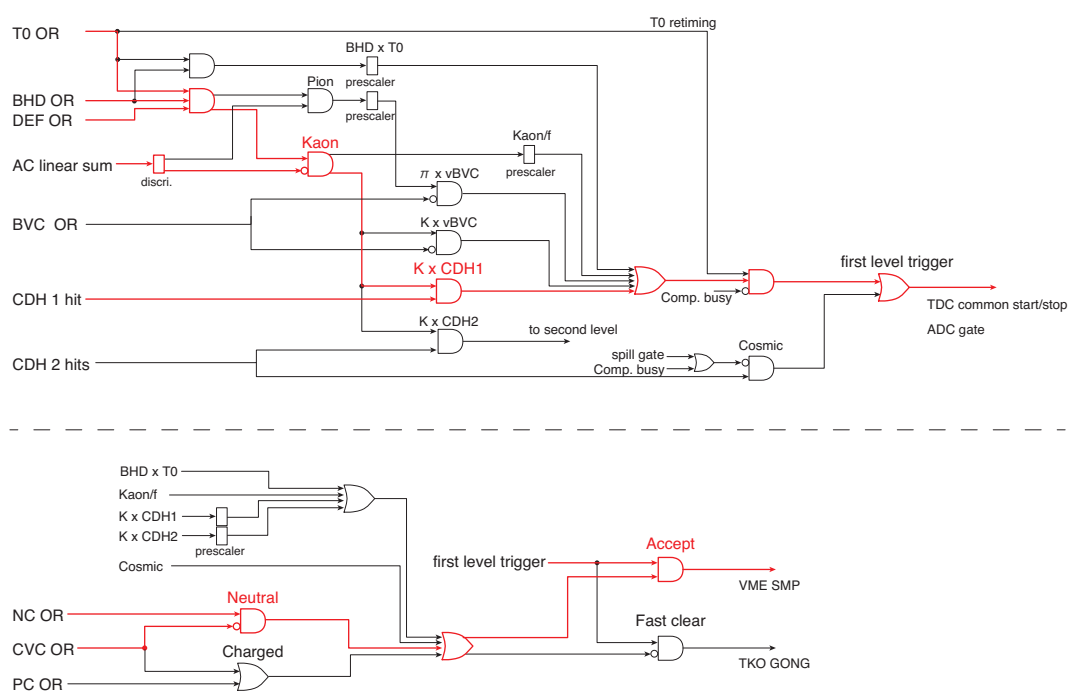


Figure 2.12: Schematic view of trigger scheme

# Chapter 3

## Data analysis

### 3.1 Over view

This chapter describes data analysis. First, the general analysis method for hodoscopes and drift chambers will be described. Next, the analysis of beamlines is described. In this analysis, kaon is selected and accidental events, such as the passage of two particles, are eliminated to define the beam irradiated to the target. The number of irradiated beams is calculated from the scaler and the luminosity is calculated using the beam survival rate DAQ efficiency and the trigger efficiency.

Next, the CDS is explained. The CDC performed tracking of decayed particles in the solenoid magnet and decided reaction vertex with the beamline chamber which is called the BPC. The CDH measured the timing of decayed particles and identified these particles with momentum reconstructed by CDC. The efficiency of the CDC was measured using the CDH and the IH which were installed at the outer and the inner of the CDC as trigger counters.

Next, forward detectors were explained. These were divided into the forward charge particles and forward neutral particles. The beam was swept to the Beam Dump. Forward scattered particles were detected by the Neutron Counter (NC), the Charge Veto Counter (CVC), and the Proton Counter (PC). Positive charge particles were swept to the opposite direction of the beam, so the PC was placed about 15m downstream of this direction. Although the purpose of the CVC is to veto for neutral particles, half of this counter was used detection of positive particles scattered forward to cover the high momentum region. Because these particles were bent, the Forward Drift Chamber (FDC1) was installed between the target system and the Ushiwaka magnet. The trajectory of the forward charge particle was determined using the reaction vertex point, the position before bent, and counter hit position. The particle identification of a forward charged particle was performed using the momentum estimated from the bending angle and

velocity calculated from the T0-PC TOF. And, the momentum of forward scattered proton was finally calculated from the TOF method due to the high resolution. The efficiency of the forward proton was evaluated using the  $d(K^-, (\pi^- \Lambda)_{CDS})^* p$  reaction which was searched in events detecting 2 protons and  $\pi^-$  by the CDS. We selected the  $d(K^-, p)^* \pi^- \Lambda$  and the  $d(K^-, p)^* \pi^- \Sigma^0$  final state from missing masses, which were corrected the acceptance that evaluated using the Monte Carlo simulation. After that, were converted to the cross section using conversion factors that consist of the luminosity and detector efficiencies.

Because forward scattered neutral particles straightly go to the NC, the momentum of the forward neutral particle was measured by the TOF method. The flight length was determined from the counter position and the vertical position which was estimated from the time difference of the up and the down PMT. The contamination from the charged particles were rejected by the BVC and the CVC which were install just upstream of the Ushiwaka magnet and the NC. We also adopt the energy deposit threshold for the rejection of accidental events which was estimated from the S/N ratio and purity of the neutron at the Quasi-elastic region. The efficiency of the NC system was decomposed to the two parts, whose one is the intrinsic efficiency and the other is the over veto ratio by the BVC and the CVC. The intrinsic efficiency was estimated from the  $K^- p \rightarrow K^0 n$  reaction using the hydrogen target data. On the other hand, the over veto of the BVC and the CVC probably depend on the beam condition, so the ratio was estimated using the production data. We identified the  $d(K^-, n\pi^+\pi^-)^* n$  final state, and this final state was decomposed to the  $k^0$  production, the  $\Sigma_{forward}$  production, and the  $d(K^-, n)^* \pi^\mp \Sigma^\pm$  state. The  $d(K^-, n)^* \pi^\mp \Sigma^\pm$  state includes two charge modes, which were decomposed at the bin-by-bin of the  $d(K^-, n)^* X$  spectrum. The decomposition of these modes was used to the templates that generated from the Monte Carlo simulation. The  $d(K^-, n)^* K^0 n$  spectrum and the  $d(K^-, n)^* \pi^\mp \Sigma^\pm$  spectra were corrected the acceptance of the CDS using the MC simulations and were converted to the cross sections using the conversion factor which consists of the luminosity and the detector efficiencies.

### 3.1.1 Basical calibration

Hodoscope signals were read out as ADC and TDC data and chambers were read out only TDC. TDC data was converted to time. The parameters for this were calibrated using time calibrator. That module outputs two signals with a time difference of a certain constant multiple of time.

Hodoscope had a correlation between ADC and time as shown in the left of Figure.3.1 due to the rising edge of the signal. The correlation was corrected as shown on the right of Figure.3.1 by the follow function.

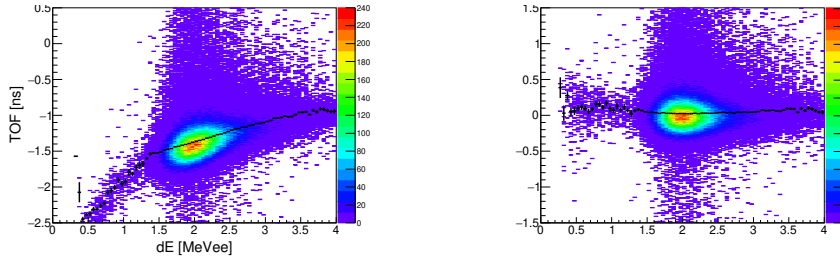


Figure 3.1: These figures indicate about slewing effect correction. These figures show the energy deposit of the T0 as the horizontal axis and the calculated time shift of T0-NC by the  $\gamma$ -ray as the vertical axis. The left figure shows about before correction, and the right figure shows about after correction.

$$t_{corrected} = p_0 + p_1 \frac{t}{\sqrt{dE}} + p_2 t$$

This collection was performed using a well-known timing signal. For example, the Fig3.1 shows the correction of the T0 using the  $\gamma$ -ray peak of the T0-NC TOF which has constant velocity. This peak is also shown in Fig3.35.

Timing data of drift chambers was used to convert to the drift length. The above figure of Fig3.2 shows the drift time distribution of the drift chamber installed at the beamline. The middle figure indicates differentiated distribution which was used to decision start timing of each channel. The bottom figure indicates integrated distribution which corresponds to conversion map from the drift time and the drift length by assumption that beam was uniformly irradiated on.

## 3.2 Beam line

### 3.2.1 DAQ live rate and trigger efficiency

The DAQ live ratio was evaluated by the ratio of the number of accepted events to the number of 1st trigger requests. For MR-RUN78, these values for all runs are plotted in Figure.3.3.

$d(K^-, n)$  and  $d(K^-, p)$  trigger efficiencies were evaluated by the offline analysis in which trigger decomposed two-step. The first part is  $K \otimes CDH1$  which was estimated using unbiased Kaon trigger. The second part is  $neutral=NC \otimes CVC \otimes BVC$  or  $charge=PC \cup CVC_{half}$  which was estimated using the unbiased  $K \otimes CDH1$  trigger. Figure.3.4 shows about trigger efficiency.

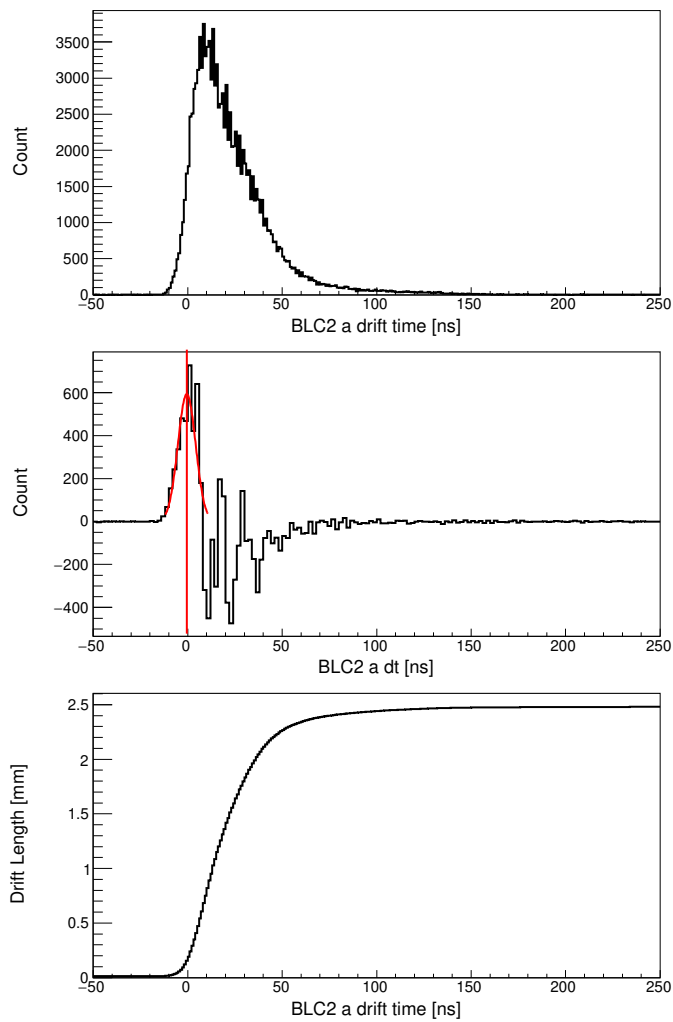


Figure 3.2: These figures indicate the calibration of drift chambers. The above figure shows raw distribution. The middle figure shows the start timing decision which is indicated by red lines. The bottom figure shows the  $x$ - $t$  map.

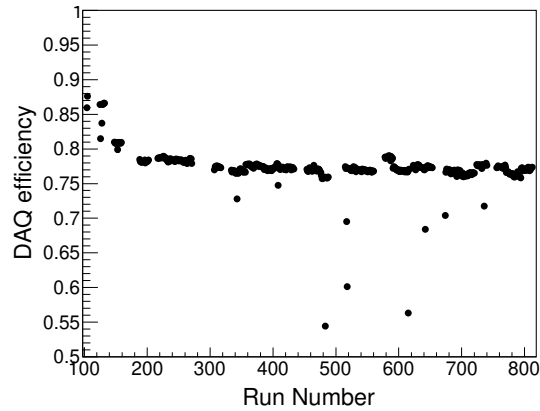


Figure 3.3: This figure shows DAQ live rate of production run in MR-RUN79.

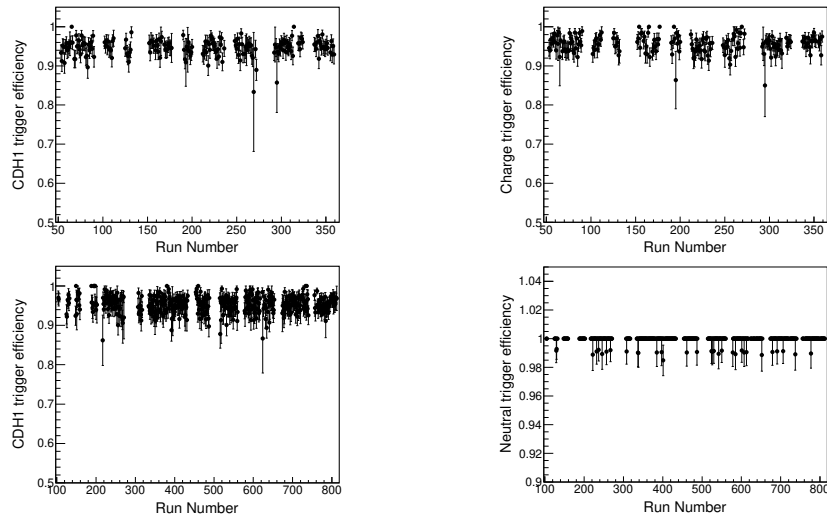


Figure 3.4: These figures show about trigger efficiencies in each run. The above figure represents MR-RUN69 used in the  $d(K^-, p)$  analysis. The left figure shows the  $K \otimes$  CHD1 trigger and the right figure shows the charge trigger. The bottom figure represents MR-RUN78 used in the  $d(K^-, n)$  analysis. The left figure shows the  $K \otimes$  CHD1 trigger and the right figure shows the neutral trigger.

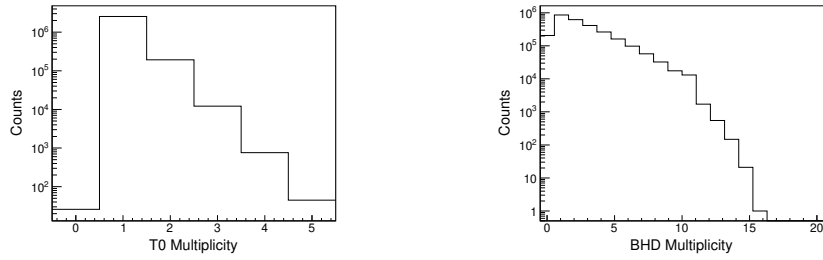


Figure 3.5: These figures show the multiplicity of T0 and BHD counter.

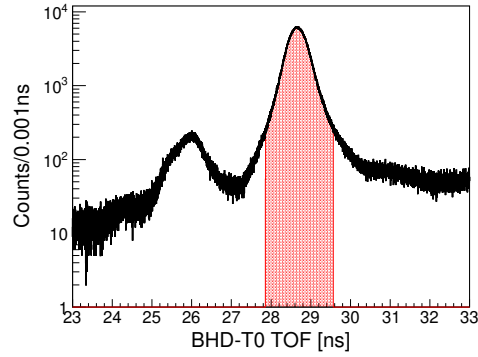


Figure 3.6: BHD-T0 time-of-flight with 7.7m flight length. The red hatched plot indicates an acceptable region as a kaon.

### 3.2.2 T0 and BHD analysis

T0 counter was installed at just upstream of the CDC to define the start timing of all detectors. So, we require 1 hit of the T0 counter. The BHD counter was installed to define beam particle by time-of-flight method with 7.7m flight-length. Fig[3.5] represents the multiplicity of T0 and BHD counter. Because BHD multiplicity has many events that are not 1hit, we don't require BHD 1hit. Fig[3.6] represents T0-BHD time-of-flight with the on-line kaon trigger, which looks clear kaon peak around 29ns. The peak around 26ns seems pion, which come from the RF structure and the strange beam trajectory, and so on. The red hatched region indicates the selection of the kaon beam.

### 3.2.3 Beam line chamber

BLC1 and BLC2 were installed upstream and downstream of the D5 magnet, respectively to measure beam momentum using the transfer matrix of the D5 magnet. These are planer the type drift chamber whose drift length was calculated using the X-T map, which was the integration of drift time. The track time of BLC was estimated from timing signals of pair plane due to constant drift length. SX beam has RF-structure seems like the center

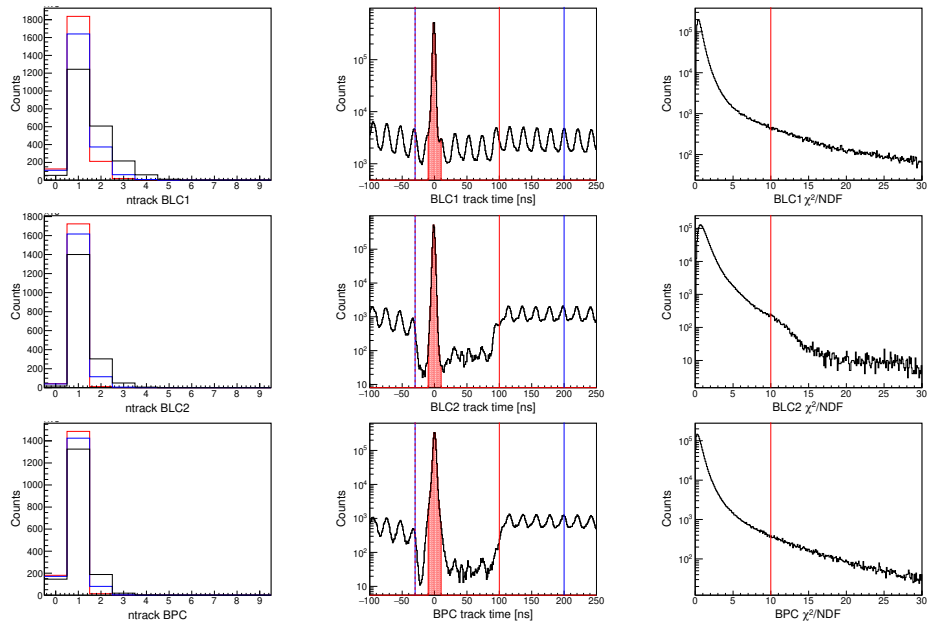


Figure 3.7: The left, the middle and the right figures show the number of tracks, track time and  $\chi^2/NDF$ , respectively. Color plots in the left figure indicate some time window. The above, the middle and the down figures represent BLC1, BLC2 and BPC, respectively. The BPC was described after.

figures of Fig3.7, so we select synchronization about beam which indicates the red hatched region. The left figures represent the number of tracks, in which black, blue, and red indicate time window of all,  $-30 \sim 100[\text{ns}]$ , and  $-30 \sim 200[\text{ns}]$ , respectively. We select 1track events in red time window selection to keep statistics. The right figures show  $\chi^2/NDF$  distribution after 1track selection. We accepted  $\chi^2/NDF < 10$  events as good track.

### 3.2.4 Beam momentum analyzer - D5 magnet

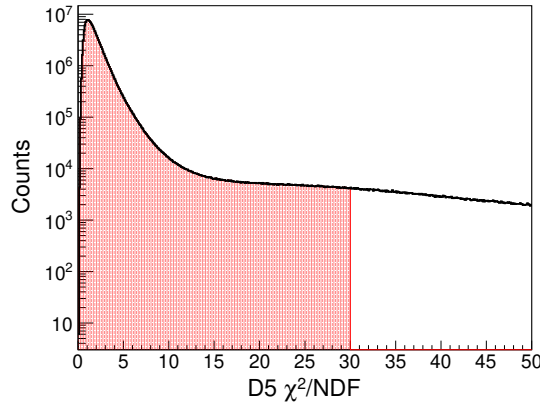


Figure 3.8: This figure shows the connected trajectory of BLC1 and BLC2 using the D5 transfer matrix. The red hatched region represents an acceptable region.

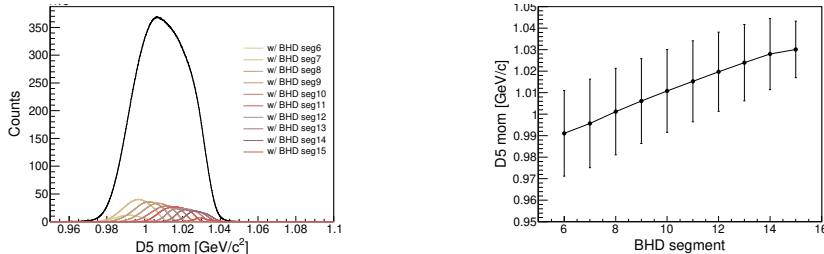


Figure 3.9: The left figure shows beam momentum. color plots indicate distributions tagged the BHD segment in BHD multiplicity one event. The right figure represents center value of momentum as points and matching region as bars.

Beam particle momentum was calculated by connecting the BLC1 track and the BLC2 track using the transfer matrix of the D5 magnet. The  $\chi^2/NDF$  of connection trajectory was shown as Fig3.8. We accept  $\chi^2/NDF < 30$  events. Calculated beam momentum distribution is shown as Fig3.9, which is seen in the relation between beam momentum and BHD segments.

So, we require  $3\sigma$  level matching between beam momentum and BHD segment, which is shown as the right figure.

### 3.2.5 BLC2-BPC matching

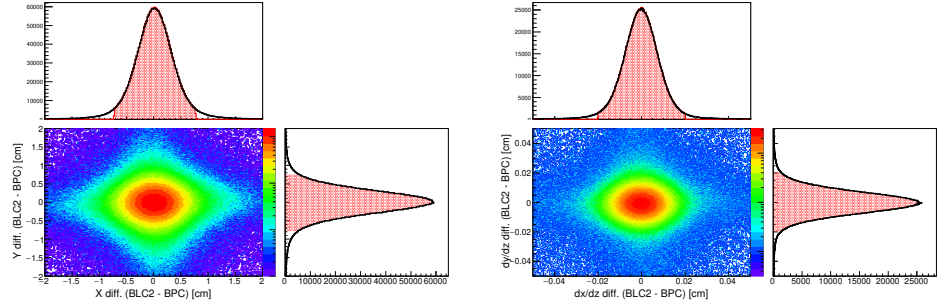


Figure 3.10: These figures indicate the connection between the BLC2 and the BPC. The left figure shows about position matching at the center of these. The right figure shows direction matching. The red hatched region indicated an acceptable region.

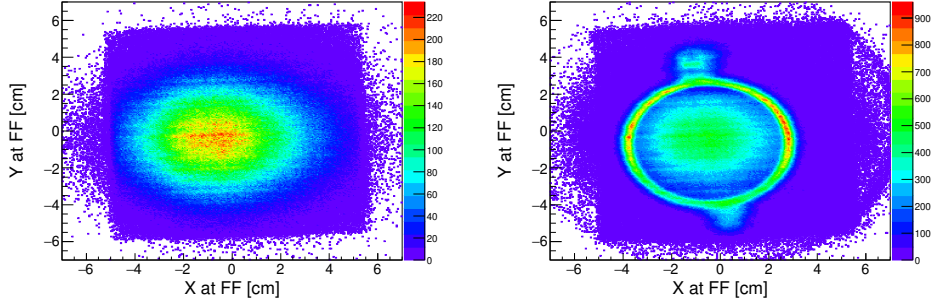


Figure 3.11: These figures shows beam profile at FF. The left figure shows about the unbiased kaon trigger. The right figure shows about CDH2 hit trigger.

The BPC is the same type drift chamber as BLC1/2, so the analysis of itself is the same as BLC1/2, which is shown in Fig3.7. There is no magnet between the BLC2 and the BPC, so trajectories reconstructed by them should be successfully connected within multiple scattering and resolution. There are many materials between the BLC2 and the BPC, for example, the T0, the AC, BPD, and air, also direction ( $dx/dz$  or  $dy/dz$ ) resolution affects on extracted position resolution. The  $z$  length ratio of these is  $(\text{BPC } z)/(\text{BLC2 } z)=50.4\text{mm}/310\text{mm}\sim 1/6$ , so extracted position resolution was almost decided by the BPC. On the other hand, materials were placed at just down stream of the BLC2 for example the T0 and the AC. These two effects were estimated almost the same, so we evaluated position matching

at the center of the BLC2 and the BPC as Fig3.10. We also require direction matching the right figure of Fig3.10. The BPC also defines The beam profile at the experimental target position as shown in Fig3.11. The profile required reaction at the trigger level was clearly seen target cell. The red circle indicates an acceptable region as an effective kaon beam.

### 3.2.6 Luminosity

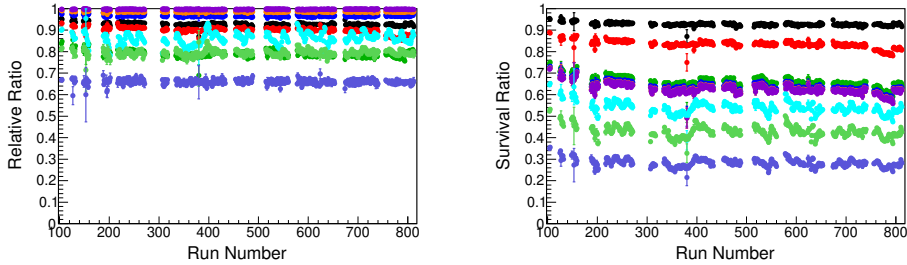


Figure 3.12: Left and right figure indicates run dependence of relative and survival ratio in MR Run78, respectively. Relative ratio means ratio against before condition. Survival ratio means ratio from all K/f trigger events.

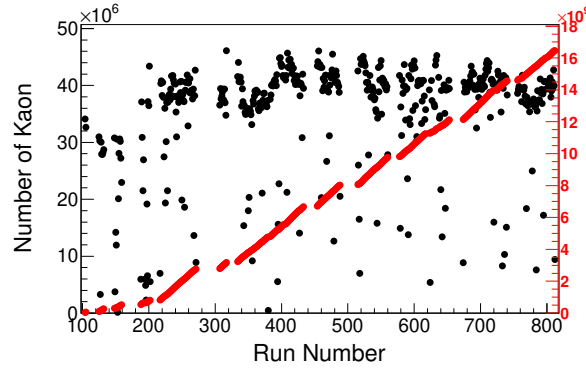


Figure 3.13: This figure shows kaon number irradiated on the liquid- $D_2$  target.

The Kaon number of trigger levels is counted by the scaler DAQ, which also includes inaccurate events due to mixing of  $\pi$ , 2-particles, and strange trajectories, as well as transformations and scattering on the beamline. To avoid these events, a number of selections are made as described above. The following is a list of beamline selections.

1. T0 1hit selection

Table 3.1: Summary table of  $d(K^-, p)$  scaling parameters

Component	value	error	value	error
Luminosity ( $/\mu b$ )	2478	81	10	
Target Length (cm)			0.1624	0.0014
Target density [ $g/cm^3$ ]			$2.05 \times 10^{10}$	
Number of Kaon			0.336	0.0001
Survival ratio of $K^-$			0.821	0.0001
DAQ live ratio				
Trigger efficiency				
$K \otimes CDH1$			0.9527	0.0003
Charge			0.9559	0.0004
Efficiency of the CDC	0.977	0.04		
Efficiency of the forward detectors	0.819	0.042		

2. T0-BHD TOF kaon selection
3. BLC1 1track selection
4. BLC2 1track selection
5. D5 momentum reconstruction
6. D5 and BHD matching selection
7. BPC 1track selection
8. BLC2 and BPC connection
9. Beam on target at FF

These values is shown in Fig3.12. Number of kaon irradiated on the liquid- $D_2$  target is shown in Figure.3.13. These values, together with the DAQ and trigger efficiencies described in the Section3.2.1, are evaluated as luminosity, as shown in the Table.3.1 and 3.2. Data were collected on MR-Run69 for forward protons and MR-Run78 for forward neutrons.

### 3.3 CDS

The CDS analysis is preformed below procedure

1. CDC tracking
2. Seach associated CDH (IH) hit.
3. Defining reaction vertex point and particle identification.

Table 3.2: Summary table of  $d(K^-, n)$  scaling parameters

Component	value	error	value	error
Luminosity (/ $\mu b$ )	5927	158	10	
Target Length (cm)			0.1613 – 0.1617	0.0015
Target density [ $g/cm^3$ ]			$5.83 \times 10^{10}$	
Number of Kaon			0.281	0.0003
Survival ratio of $K^-$			0.768	0.0021
DAQ live ratio				
Trigger efficiency				
$K \otimes \text{CDH1}$			0.9527	0.0004
Neutral			0.9992	$6.7 \times 10^{-6}$
Efficiency of the CDC	0.977	0.04		
Efficiency of the NC	0.291	0.015		
Intrinsic the NC			0.317	0.016
Over veto of the CVC/BVC			0.081	0.007

#### 4. Re-fitting of CDC using $\beta$ of particle

In this section, these analysis procedure is explained.

##### 3.3.1 CDC tracking

The CDC tracking was performed in uniform magnetic field, so its track is helix track which was introduced by K.Fuji [53] as following equations.

$$x(\phi) = d_\rho \cos \phi_0 + \frac{1}{\rho} (\cos \phi_0 - \cos(\phi_0 + \phi)) \quad (3.1)$$

$$y(\phi) = d_\rho \sin \phi_0 + \frac{1}{\rho} (\sin \phi_0 - \sin(\phi_0 + \phi)) \quad (3.2)$$

$$z(\phi) = d_z - \frac{1}{\rho} \tan \lambda \dot{\phi} \quad (3.3)$$

where  $d_\rho$  is the distance of the helix from the origin point in the  $xy$  plane,  $d_z$  is distance of  $z$  direction,  $\phi_0$  is the azimuthal angle to  $z$ -axis,  $\lambda$  is elevation angle and  $\rho$  is the inverse of the radius of the helix.

In this parametrization, charged particle momentum is represented as below,

$$\mathbf{p} = \frac{cB}{\rho} \begin{pmatrix} -\sin(\phi_0 + \phi) \\ \cos(\phi_0 + \phi) \\ \tan \lambda \end{pmatrix} \quad (3.4)$$

where  $c$  is the light velocity,  $B$  is strength of uniform magnetic field in the  $z$  direction.

Drift time convert to drift length using fifth order polynomial function which function was iteratively adjusted to minimize systematic shift. Fig3.14 shows drift time and drift length.

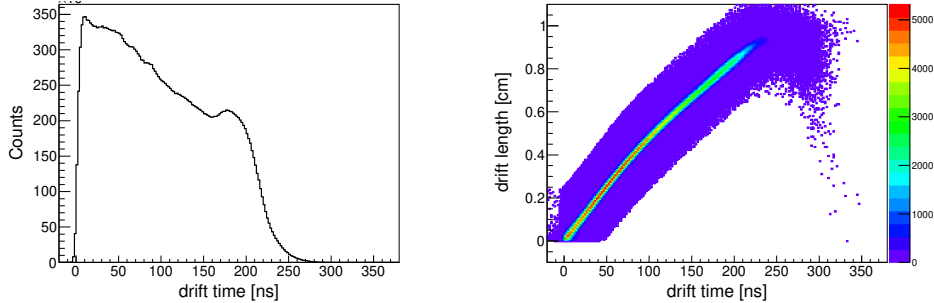


Figure 3.14: Left figure shows drift time distribution of CDC. Right figure shows relation of drift time and drift length.

### 3.3.2 CDH

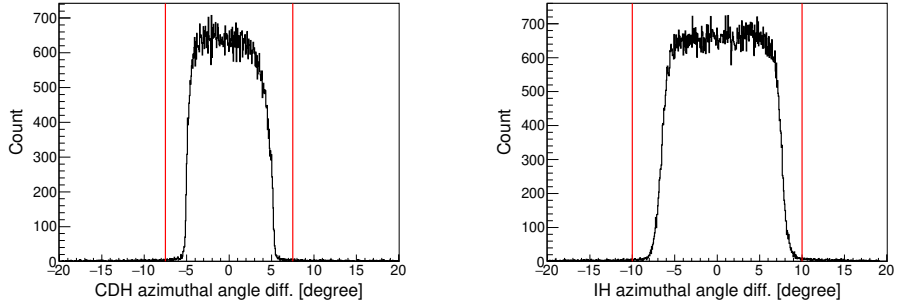


Figure 3.15: Left figure shows azimuthal angle difference the CDH hit segment and the CDC tracking. Right figure shows azimuthal angle difference the IH hit segment and the CDC tracking. The CDH and the IH segment size are  $\pm 5^\circ$  and  $\pm 7.5^\circ$ , repectively. Acceptable region indicates red lines.

The CDH was installed outer side of the CDC and The IH was installed inner side of CDC. The CDH and IH hit position can defined exported trajectory by the CDC like Fig3.15. The CDH and the IH have 36 and 24 segments, respectively which correspond to 10 degree and 15 degree of azimuthal angle. CDC track and CDH or IH hit within  $\pm 7.5^\circ$  and  $\pm 10^\circ$  are associated, respectively. Fig3.15 shows azimuthal angle matching of the CDC and the CDH and the IH.

The CDH timing infomation is used to identify of the particle. The flight length of the T0 to the CDH is calculated in two parts, one is the T0 to the reaction vertex point which was evaluated and next is the reaction vertex point to the CDH hit position.

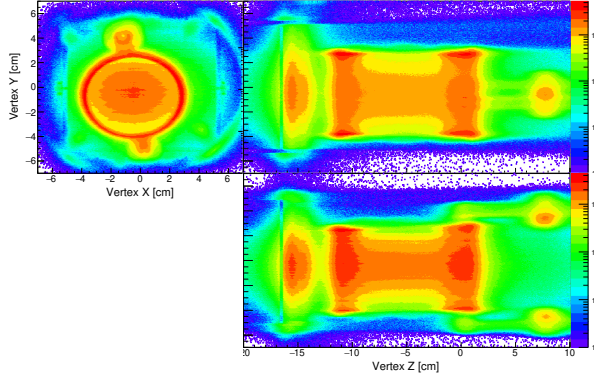


Figure 3.16: Reconstructed vertex point distribution by the BPC and CDC. Right figure shows about  $xy$  plane. Up figure and down figure of lift side was shows  $yz$  plane and  $xz$  plane, respectively.

### 3.3.3 Vertex reconstruction

The reaction vertex point was calculated from the beam track by the BPC and the CDC tracks. First, the CDC track which gives the distance of the closest approach (DCA) was searched and the reaction vertex point was defined by closest point of the beam track. Fig3.16 shows reconstructed reaction vertex images. We used the target chamber with  $6.8\text{cm}$  diameter PET whose image was clearly shown in  $xy$  plane figure.  $D_2$  target transfer pipes placed parallel to the floor was shown at  $z = 8\text{cm}$  in light side figures, also DEF counter installed just upstream of the target chamber was seen at about  $z = -15\text{cm}$ .

For evaluation of the vertex resolution, some projected histograms was made. The  $xy$  vertex resolution was evaluated at some range of  $z$  axis and target center of  $y$  as left figure of Fig3.17. The  $xy$  vertex resolution was evaluated about  $1.4\text{mm}$ . The  $z$  vertex resolution was evaluated by the DEF counter using  $z$  axis projection histogram at  $r < 3\text{cm}$ . The  $z$  vertex resolution was evaluated about  $7.0\text{mm}$ .

### 3.3.4 Particle identification

Decay particle was identified by the velocity calculated from the T0-CDH time-of-flight and the momentum evaluated from the curvature of magnetic field. The velocity  $\beta$  was calculated using below equation

$$\beta = \frac{1}{c} \frac{L_{\text{Vertex-CDH}}}{(TOF_{\text{CDH-T0}} - T_{\text{T0-Vertex}}^{\text{calc}})} \quad (3.5)$$

The  $L_{\text{Vertex-CDH}}$  is the flight-length from the T0 to the CDH, which was calculated from line distance from the the T0 to the reaction vertex and

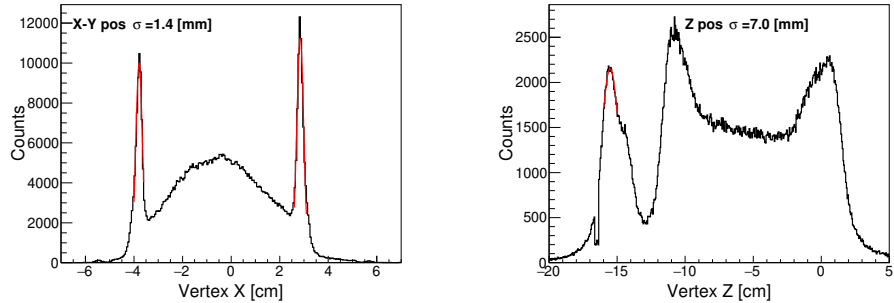


Figure 3.17: Left figure shows x axis projection at  $y = 0\text{cm}$  and  $z > -12.5\text{cm}$  to evaluate  $xy$  vertex resolution. Right figure shows z axis projection at  $x^2 + y^2 < 3\text{cm}$  to evaluate  $z$  vertex resolution.

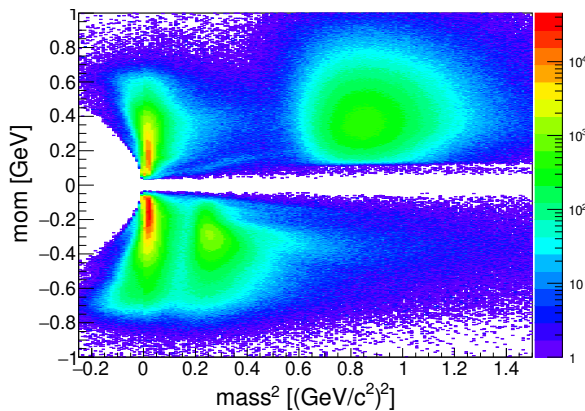


Figure 3.18: This figure shows scattered plot of mass square and momentum. Mass square was calculated by the Eq.3.6. Sign of the momentum means particle charge so, plus means positive charged particle and minus means negative charged particle.

helix distance from the vertex to the CDH hit position. The  $T_{T0-Vertex}^{calc}$  mean the calculated time from the T0 to the reaction vertex point using beam momentum analyzed by the D5 magnet with energy loss correction of the materials at beam trajectory. Decay charged particles were identified by the mass square which calculated by the Eq.3.6 and the momentum.

$$m^2 = p^2 \times \frac{1 - \beta^2}{\beta^2} \quad (3.6)$$

### 3.3.5 Time walk correction of CDC

Start timing of CDC was of cause depend on the velocity of decay particle because reach time to drift area was depend on the velocity. Actually, the correlation between residual of CDC and the  $1/\beta^2$  was seen in Fig3.19. The correlation was collected using time-walk collection like method by fitting with following function

$$t_{corrected} = p_0 + p_1\beta + p_2\beta^2 + p_3 \exp(p_4\beta). \quad (3.7)$$

This collection was adopted wire-by-wire of the CDC. Fig3.19 represents all wire summed scatter plot. The figure after collection (right) seen almost no correlation.

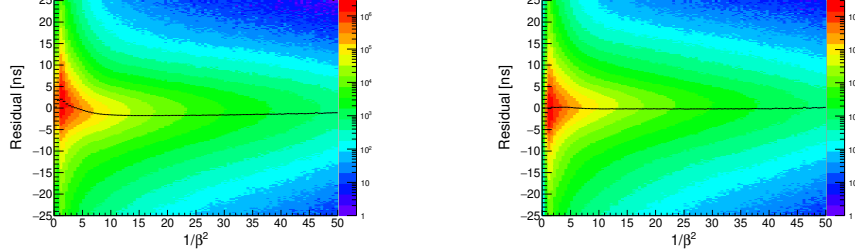


Figure 3.19: These figures show correlation between  $1/\beta^2$  and residual convert to time using dt-dx correction function. Left figure shows before time-walk collection. Right figure shows after time-walk collection.

### 3.3.6 Recunstructed hyperons by CDS

The  $K^0$  and the  $\Lambda$ , well-known hyperons decay to  $\pi^+ \pi^-$  and proton and  $\pi^-$ , respectively. These decayed particles can be identified and momentum was reconstructed by the CDS as shown in Fig3.20.

### 3.3.7 CDC efficeicny

In MR-RUN69, the IH was installed at CDS which surrounding the target cell. CDC efficiency was estimated using the IH and the CDH as trigger

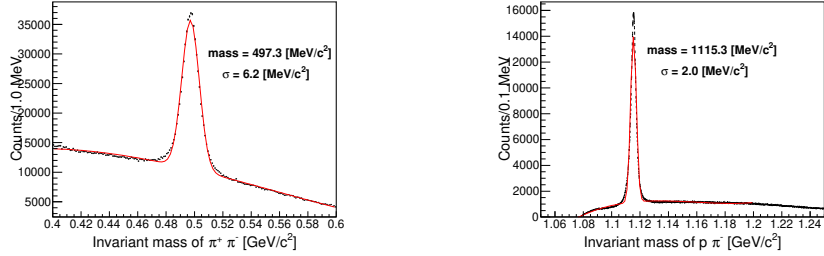


Figure 3.20: Left figure shows reconstructed  $K^0$  from  $\pi^+\pi^-$  detected by the CDS. Right figure shows reconstructed  $\Lambda$  from  $p\pi^-$  detected by the CDS. Background function was evaluated by 5-th polynomial function.

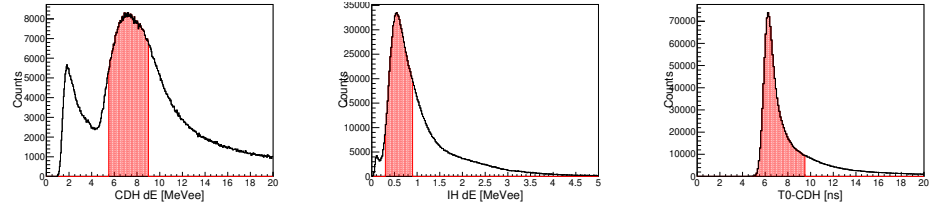


Figure 3.21: Trigger event selection for CDC efficiency. left, center and right figures show CDH dE, IH dE and T0-CDH tof. Red hatched region indicates acceptable region as pass through MIP.

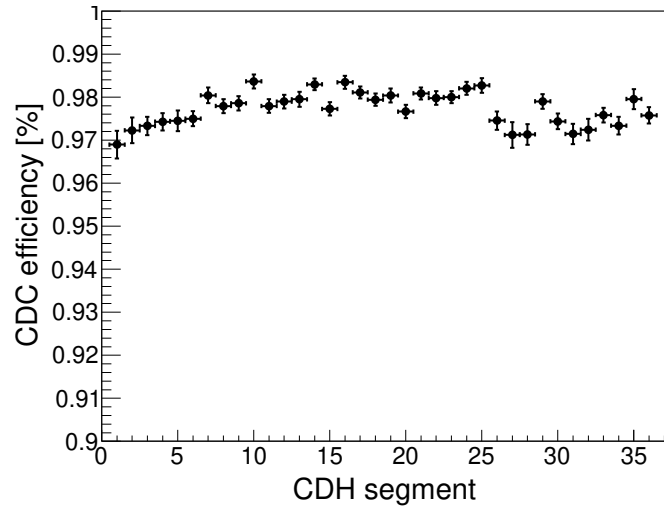


Figure 3.22: This figure plotted CDC efficiency about each CDH trigger segment.

counter. Trigger events was required particle like a MIP which was judged specific energy deposit at the CDH and the IH and fast timing at the CDH. The IH do not use timing information because single read-out and bad time resolution. The trigger event also required the CDH and The IH hit in same side which was azimuthal angle difference within 45 degree. CDC efficiency was estimated whether can be right trajectory reconstructed. Right trajectory was judged within a hodoscope size. We estimated CDC efficiency at  $97.7 \pm 0.4\%$  whose error was evaluated by fluctuation of CDH trigger segment.

### 3.4 Forward proton detectors

In this section, the analysis of detectors for the forward scattered proton was described. The forward scattered proton was detected by the PC and half of the CVC and these trajectories were determined from the reaction vertex, the position upstream of the Ushiwaka magnet, and the counter hit position. The particle identification of forward charge particles was performed by the momentum from the trajectory and the TOF of the T0 and the PC/CVC. At first, The PC and the CVC were calibrated using the special data set, in which  $1GeV/c \pi^-$  beam injected to the CVC and the PC by changing the Ushiwaka magnetic field. After that, the time offset calibration was performed by missing masses of well-known particles. The accuracy of the horizontal axis and the efficiency estimation using the  $d(K^-, \Lambda\pi^-)''p''$  events in which the  $\Lambda$  and the  $\pi^-$  were detected by the CDS was explained.

#### 3.4.1 Forward charge particle identification

The trajectory of the forward scattered charge particle was curve trajectory due to the Ushiwaka magnet. The trajectory was reconstructed from the reaction vertex point, the FDC1 position, and the counter hit position using the magnetic field map of the Ushiwaka. The field map was made by the Opera which is the software [54] of an finite element method. The actually used field map was scaled using the measured value at the center of Ushiwaka from the calculated map. The trajectory of charge particle was calculated by the the third order Rungge-Kutta method and determined to minimize the weighted residual at each position. The momentum was reconstructed from this calculation and the mass was calculated from the TOF of the T0 and the PC/CVC. The Fig.3.23 was shown the mass-square and the momentum as the vertical axis and the horizontal axis, respectively. The proton peak was clearly seen in the figure, so events whose mass-square is between 0.5-2.5 [ $(GeV/c^2)^2$ ] were accepted as the proton. The momentum of the proton was finally calculated using the TOF method which has higher momentum resolution than the momentum by the bending angle. The missing mass spectrum of the  $d(K^-, p)''X''$  was indicated in the Fig3.24.

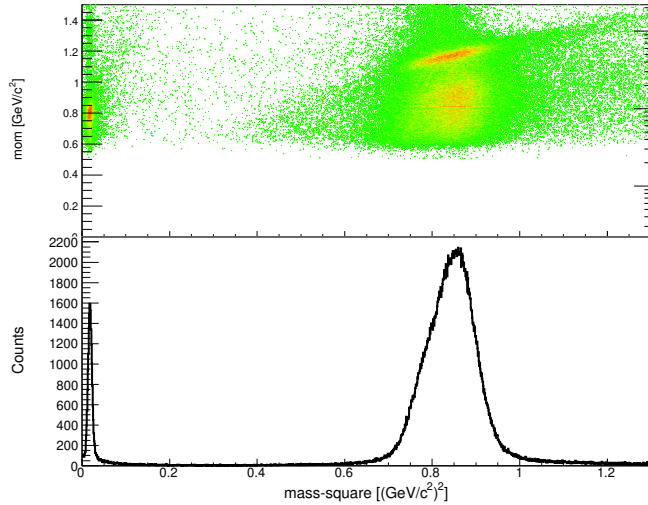


Figure 3.23: This figure shows scattered plot mass-square and momentum of forward scattered positive charged particles and horizontal axis projection (down figure). The  $\pi^+$  peak and the proton peak were seen around  $m^2 \sim 0.02[(\text{GeV}/c^2)^2]$  and  $m^2 \sim 0.85[(\text{GeV}/c^2)^2]$ , respectively.

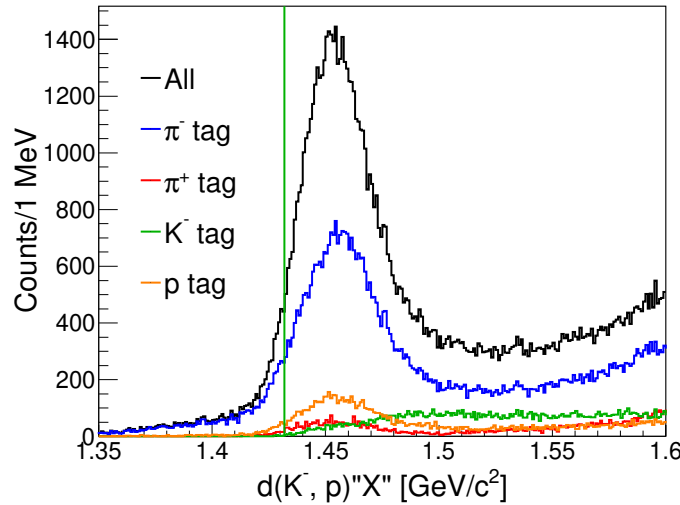


Figure 3.24: This figure shows  $d(K^-, p)"X"$  missing mass spectra. The black plot indicates whole data and color plots indicate CDS particles tagged data. These plots were adopted time offset calibration using well known particles identified by the missing mass which is described at Sec3.4.2.

### 3.4.2 Time offset turning

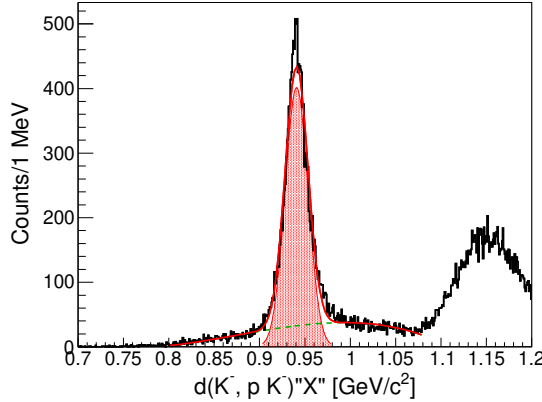


Figure 3.25: This figure shows the missing mass spectrum of  $d(K^-, pK^-)''X''$  in events detected the forward proton by the PC/CVC and the  $K^-$  by the CDS. The missing neutron peak was clearly seen. The fitting performed the Gaussian as peak and third polynomial function as the background. The red line, the red hatched region, and the broken green line indicate whole fitting line, the peak of Gaussian, and the background, respectively.

Time offset was calibrated using  $\pi^-$  beam through run for the segment by segment calibration. In that run, the  $\pi$  momentum used the value analyzed by the D5 magnet.

The shift of time offset that seems due to the ambiguity of the alignment was seen in the missing masses of well-known particles,  $d(K^-, pK^-)''n''$ ,  $d(K^-, p\pi^-\pi^-)''p''$ ,  $d(K^-, p\pi^-)''\Lambda''$  and  $d(K^-, p\pi^-)''\Sigma^0''$ . The Fig3.25 shows the missing mass spectrum of the  $d(K^-, pK^-)''X''$  in which the missing  $n$  peak is clearly seen. The other missing mass spectra were used as signals and explained in the Sec???. The calibration of these time shifts was performed to become missing masses to the PDG values. In this calibration, the beam momentum and decay particle momentum detected by the CDS was fixed and the time offset of the PC/CVC was determined to give correct masses. As a result, these missing masses were calibrated as the Fig3.26, in which black plots indicate peak position before the calibration and the red plots indicate these after the calibration, respectively. By this calibration, differences from the PDG value of these missing masses were within  $2 \text{ MeV}/c^2$ .

### 3.4.3 Horizontal axis accuracy by the $d(K^-, (\Lambda\pi^-)_{CDS})''p''$ events

The horizontal axis accuracy was also confirmed using the  $K^- + d \rightarrow p + \Lambda + \pi$  reaction. For this, the  $d(K^-, (\Lambda\pi^-)_{CDS})''p''$  events were searched from

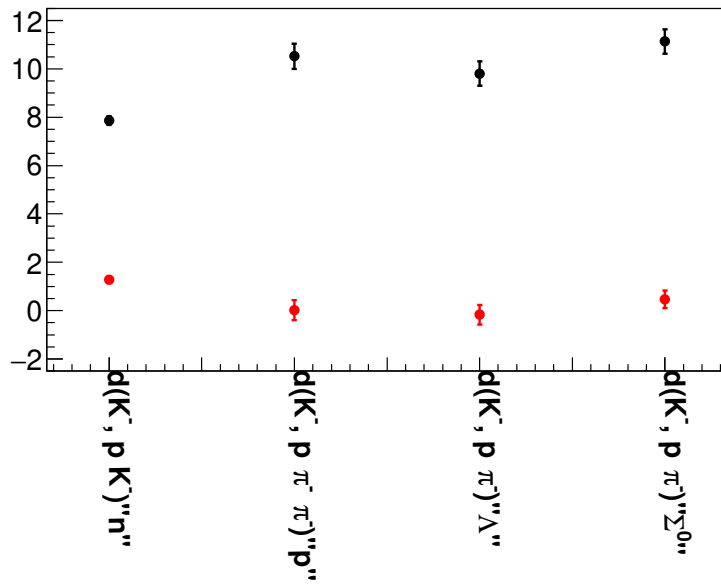


Figure 3.26: The figure indicates differences from the PDG value of missing masses of well-known particles. The black plot and the red plot indicate missing masses before and after the calibration, respectively.

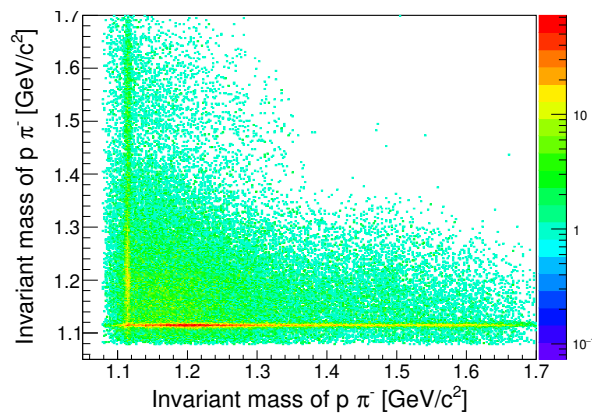


Figure 3.27: This figure shows 2-D plot of  $p\pi^-$  invariant masses. The horizontal axis represents about near DCA pair and the vertical axis represents about the other pair.

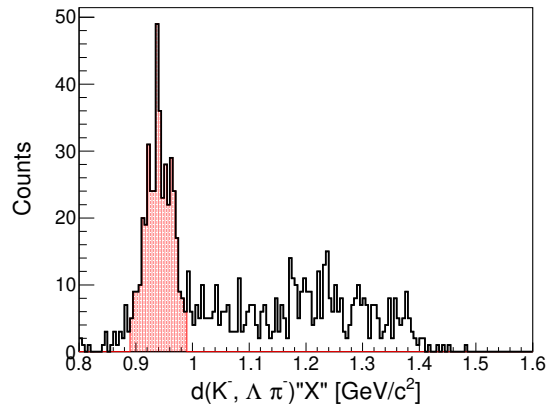


Figure 3.28: This figure shows the missing mass of  $d(K^-, \Lambda\pi^-)$  in events  $\Lambda$  and  $\pi^-$  was detected by the CDS. The red hatched region indicates the selection region as missing proton.

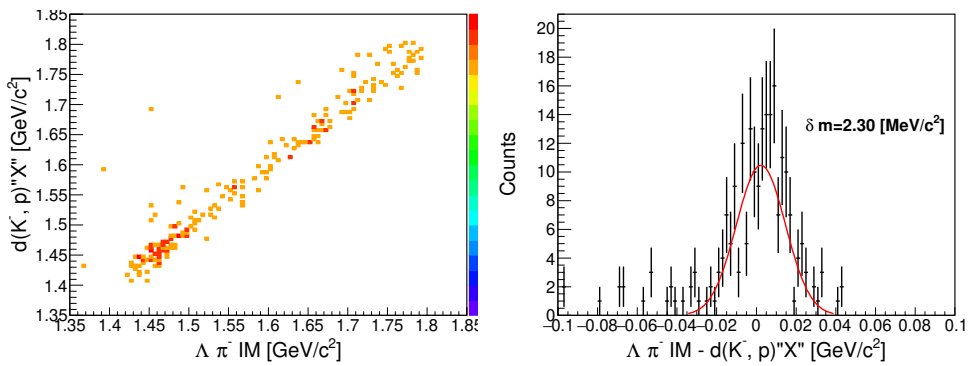


Figure 3.29: These figure indicate relation of  $d(K^-, p)''X''$  and  $\Lambda\pi^-$  invariant mass in events which detect  $\Lambda$  and  $\pi^-$  by the CDS and  $p$  by the PC/CVC. Left figure shows scatter plot and right figure represents subtraction distribution from invaraint mass to  $d(K^-, p)''X''$ .

events in which  $2\pi^-$  and the proton were detected by the CDS. And the  $\Lambda$  reconstructed from the  $\pi^-$  and the proton in these events which was shown as Fig3.27. Next, the  $d(K^-, p)\Lambda\pi^-$ "p" events were identified as the Fig3.28 which was indicated red plot.

Fig.3.29 represents the correlation of the  $\Lambda\pi^-$  mass in events analyzing the forward proton additionally above contition. In the left figure, the vertical axis indicates the  $d(K^-, p)\Lambda\pi^-$ "ant the horizontal axis indicates the invariant mass of the  $\Lambda\pi^-$ . The right figure indicates the difference of these. That indicates the accuracy of the missing mass of the  $d(K^-, p)$  is about a few  $MeV/c^2$ .

### 3.4.4 Forward proton efficiency

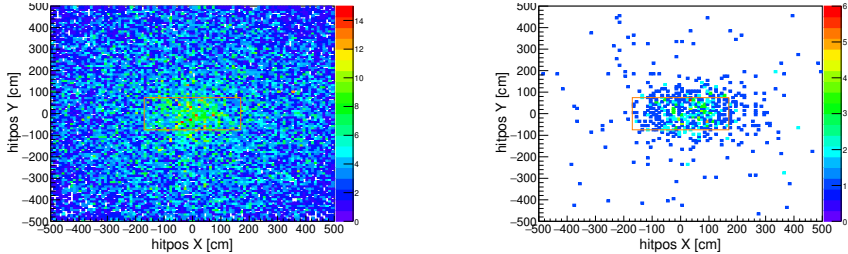


Figure 3.30: These figures show forward proton passing position calculated at the CVC. Right figure shows all events and left figure shows with events fired CVC or PC.

The efficiency of the proton was scattered to forward angle was estimated using MR-RUN78. The emmited proton was defined by the CDS as Sec.3.4.2. In this purpose, sample events must be unbaised, so we used unbaised CDH3 trigger events as events samples. The emmittion angle can be calculated from the masured particles as Fig.3.30. Because the proton scattered forward angle was bended by the Ushiwaka magnet, the efficiency of the proton maybe depends on the momentum of this. Therefor, in our interest region, that seemsed almost flat value that was guranteed by the MC sim and this effect convolved to the solid angle of the forward detectors, which discribed at Sec.??.

Fig3.32 indicates the relation of the selection region at CVC and the efficiency of forward detectors. The selection region was estimated calculated hit position of z position at CVC using a straight line. The selection region was not considered bending angle due to the Ushiwaka, becaouse the effect was evaluated using the MC sim which was described Sec.?. The efficiency was saturated at the position is  $-30$  cm, so we evaluated the efficiency was  $0.819 \pm 0.042$ .

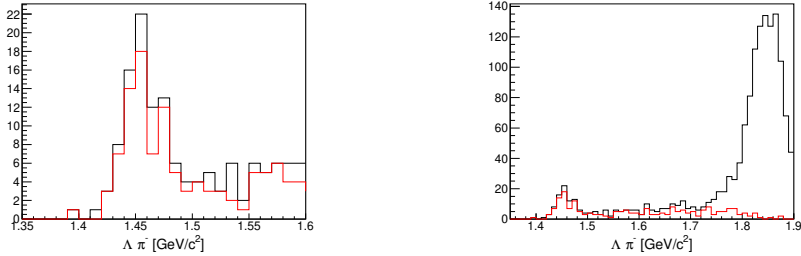


Figure 3.31: These figures shows invariant mass of  $\Lambda \pi^-$  that is cut by the size of counter is  $-30$  cm. Left figure indicates around the region of interest and right figure indicates whole regtien. Black line indicates no selection and red line indicates with PC or CVC is fired events. Efficiency seems to be drastically dropped from  $1.7 \text{ GeV}/c^2$ .

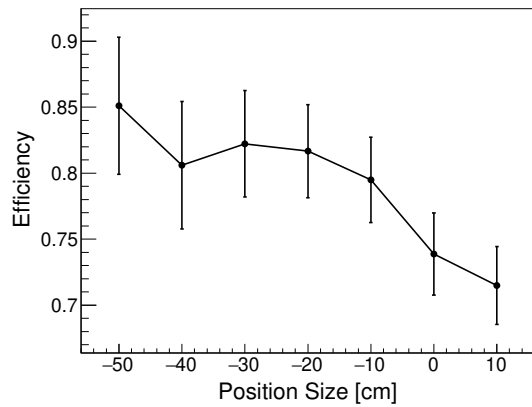


Figure 3.32: This figure shows the efficiency of forward detectors in each selection region at the CVC position. Error bars indicate statical error for the number of events.

### 3.5 Forward neutron detector system

#### 3.5.1 Neutron Counter

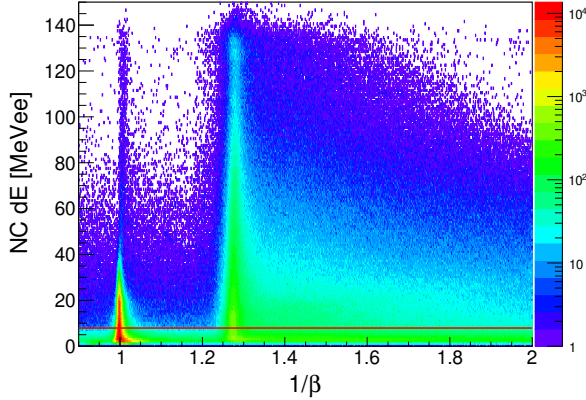


Figure 3.33: This figure shows a scattered plot of  $1/\beta$  and energy deposit.  $\gamma$ -ray events was observed at  $1/\beta = 1$ . The locus at  $\beta = 1.3$  corresponds to quasi-elastic scattering events.

Neutral particles scattered forward direction was not bent by the Ushiwaka magnet and was detected by the NC. The BVC rejected the charged particle just upstream of the Ushiwaka, whose purpose was mainly caused by the beam. Also, the CVC rejected the charged particle just upstream of the NC, whose purpose was the guarantee that the particle was neutral just before the NC. The flight-length was calculated from the reaction vertex point and the hit position of the NC. The hit position of the x-axis was determined from the counter placed position. The hit position of the vertical axis was calculated from the effective light velocity of the NC and timing signal difference of the up and the bottom PMT. The effective light velocity was evaluated using a  $^{90}\text{Sr}$  source measurement changing the position. The hit position of the z-axis was used as the center of the counter because the reaction point was unknown due to the neutral charge. The time-of-flight was evaluated from the timing of the T0 and the NC to subtract the time-of-flight of the kaon beam. The velocity of the forward neutral particle was calculated from the flight length and the time-of-flight.

Fig3.33 shows the scatter plot of the  $1/\beta$  and energy deposit. The NC was set the threshold of a signal at  $1/10$  of MIP. A low energy deposit has many backgrounds, which was estimated in the unphysical region,  $1/\beta = 0.7 \sim 0.9$ . And purity of neutron events was estimated using quasi-elastic events ( $1/\beta 1.25 \sim 1.30$ ). These figures were shown in Fig3.34. The purity of the NC was saturated at 8MeVee, so we adopted this value as the offline threshold.

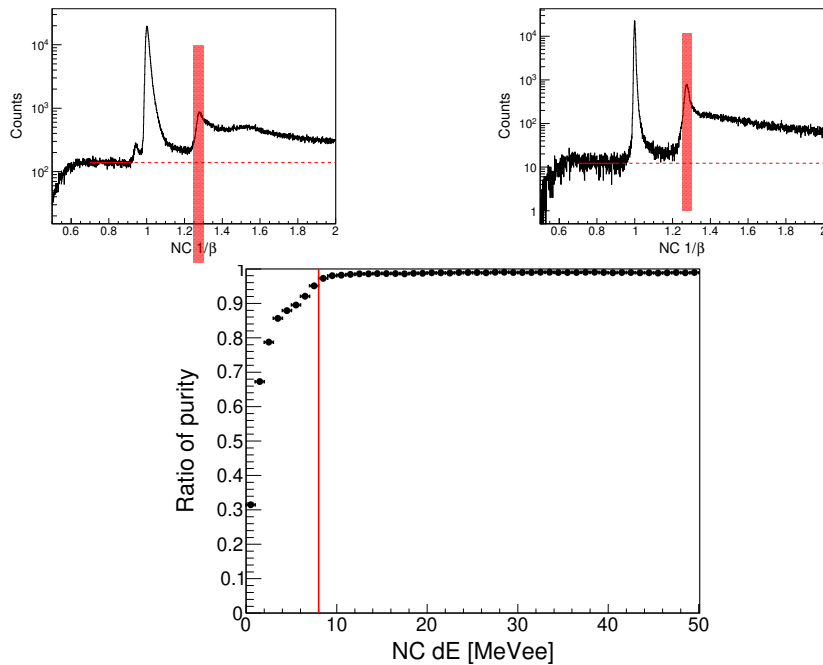


Figure 3.34: Up figures show  $1/\beta$  distribution with a specific  $dE$  range. Left figure and right figure show about  $dE = 2 \sim 3 \text{ MeVee}$  and  $dE = 8 \sim 9 \text{ MeVee}$ , respectively. The Red line indicates the background level which estimated at  $1/\beta = 0.7 \sim 0.9$ . The Red hatch region indicates a integral range as a signal.

The down figure shows the  $dE$  dependency of the ratio of signal and background. The Red line indicates 8 MeVee as the online threshold level.

The calibration of the NC was first performed using the  $\pi^-$  beam through run. In this calibration, the ADC was calibrated to the energy deposit using the MIP of  $1GeV/c \pi^-$ . The time offset was roughly calibrated using the  $1GeV/c \pi^-$  beam. These calibration runs were performed several times in the production period.

More fine tuning for the time offset was performed using a  $\gamma$ -ray which was located at  $\beta = 1$  in the production run. As a result, the resolution of the NC became about 140ps as the sum of all segments through the whole production period, which was shown in Fig3.35.

The stability was checked about time and segment. The time stability was checked to divide some period in the production period and segment stability was checked through the whole production period due to statistics, which was shown in Fig3.36.

After the calibration, the missing mass spectra were shown in Fig3.37, in which spectra tagged decay particles by the CDS also were plotted.

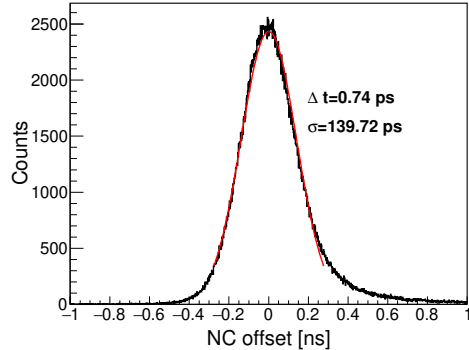


Figure 3.35: This figure shows the  $\gamma$ -ray peak in  $1/\beta$  distribution with the 8 MeVee offline threshold. Fitted gaussian was shown as red slope and mean and  $\sigma$  value was indicated at the same figure.

Fig3.36 was shows stability of the NC dureing production run and segment dependency.

### 3.5.2 NC efficiency estimation

The efficiency of the NC system was decomposed into two components which one is the intrinsic efficiency and the other is the over-veto by the BVC and the CVC. The intrinsic efficiency was measured using the  $K^- p \rightarrow K0n$  reaction with the liquid- $H_2$  target, which was the so-called MR-RUN62. Because the over-veto by the BVC and the CVC may depend on the beam status, which was estimated using the production data. In this section,

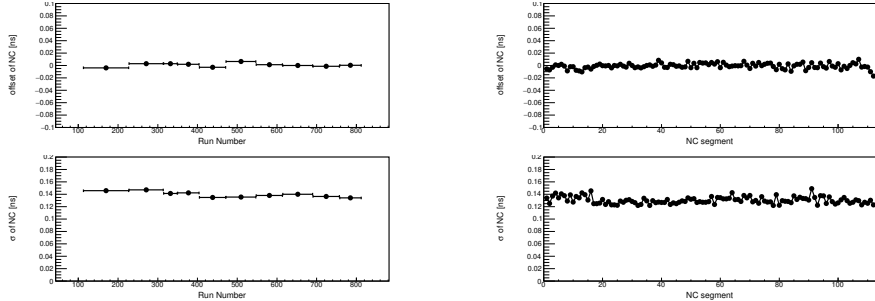


Figure 3.36: These figures show the stability of the NC performance. The above figure indicates the fluctuations of the  $\gamma$ -ray peak and the down figure indicates the time resolution of the NC. The right figure and left figures show run dependency and segment dependency, respectively.

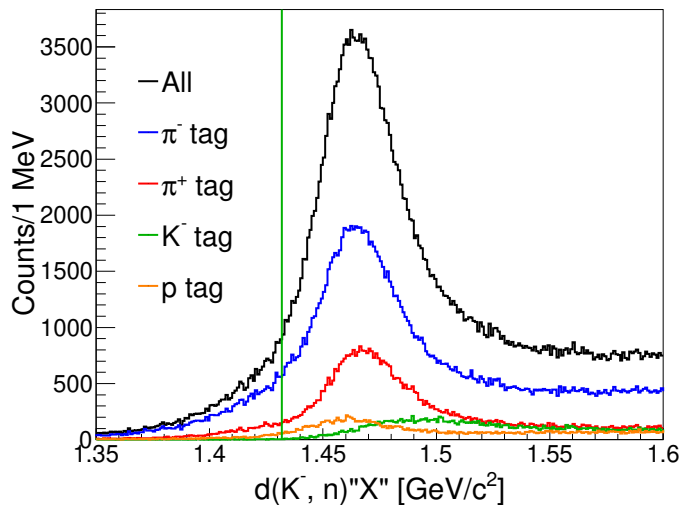


Figure 3.37: This figure shows  $d(K^-, n)^"X"$  missing mass. The black plot indicates all data and color plots indicate data with the CDS particle tag.

the intrinsic efficiency using the liquid- $H_2$  target data is explained. The candidate of the  $K^- p \rightarrow K^0 n$  reaction was searched in events detecting  $\pi^+$  and  $\pi^-$  by the CDS which may decay from the  $K^0$ . First,  $d(K^-, \pi^+ \pi^-)''n''$  events was selected as shown in Fig3.38.

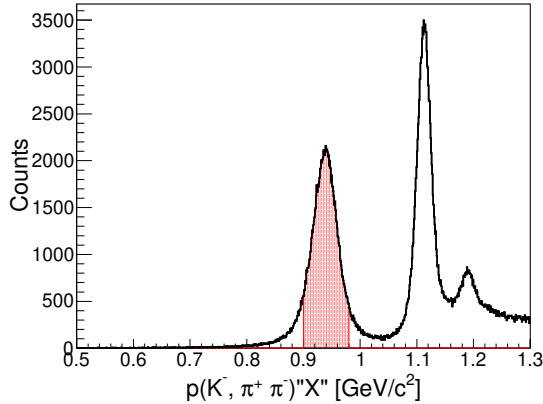


Figure 3.38: This figure shows  $p(K^-, \pi^+ \pi^-)''X''$ .  $\pi^+$  and  $\pi^-$  were detected by CDS. A peak around  $1.1\text{GeV}/c$  was due to  $d(K^-, \pi^+ \pi^-)''\Lambda''$ . The red hatched region represents the acceptable event as the  $p(K^-, \pi^+ \pi^-)''n''$ .

In this final state, the following three reactions were expected.

$$K^- p \rightarrow K^- n \quad (3.8)$$

$$K^- p \rightarrow \Sigma^+ \pi^- \quad (3.9)$$

$$K^- p \rightarrow \Sigma^- \pi^+ \quad (3.10)$$

The  $\Sigma^+$  and the  $\Sigma^-$  were identified from the  $d(K^-, \pi^-)''X''$  and the  $d(K^-, \pi^+)''X''$  as shown in the left figure of Fig 3.39. For the confirmation of  $K^0$  production and consistency of the momentum reconstruction, the  $K^0$  reconstruction was required as shown in the right figure of Fig3.39. In the same figure, the invariant mass of  $\pi^+ \pi^-$  was represented as a black plot. Form that, we see  $\Sigma$  rejections removed the background of the  $K^0$ .

The hit position at the NC of the missing neutron comes from the reaction that was reconstructed from the momenta of beam,  $\pi^- +$ , and  $\pi^-$ . That was drawn in the Fig3.40, in which the left figure shows as all events and the right figure shows events that have the NC signal. In the right figure, the NC profile is clearly seen.

Because this estimation is the measurement of the intrinsic NC efficiency, the trigger event was used the events had no signal in the CVC and the PC. The NC efficiencies were evaluated in several regions at the NC, which was shown in Fig3.41. The NC efficiencies were saturated at the NC size=  $-20\text{cm}$ , so the NC efficiency was estimated at  $0.317 \pm 0.016$  at this condition.

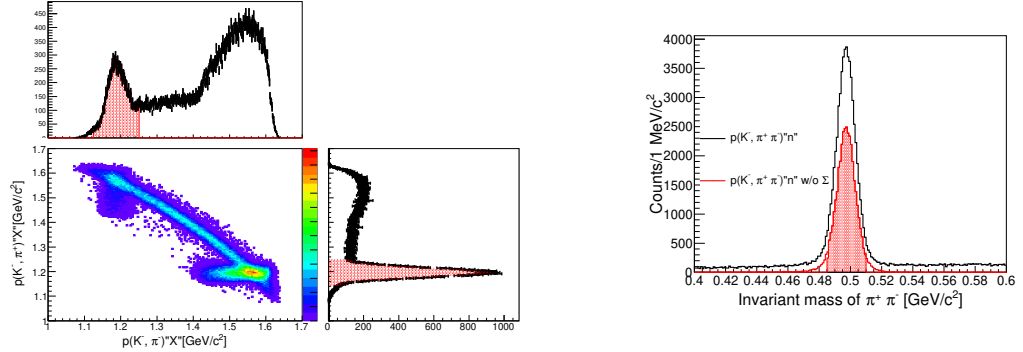


Figure 3.39: These figures show  $K^- p \rightarrow \pi^+ \pi^- n$  event decomposition. The left figure shows the scatter plot of  $d(K^-, \pi^+) X$  and  $d(K^-, \pi^-) X$ , which clearly seen " $\Sigma^-$ " and " $\Sigma^+$ ", respectively. The red hatched region indicate these selections. The right figure shows the invariant mass of the  $\pi^+ \pi^-$ . The black plot indicates no selection and the red plot indicate  $\Sigma$  rejected event. The red hatched region indicates the acceptable region as the  $K^0$ .

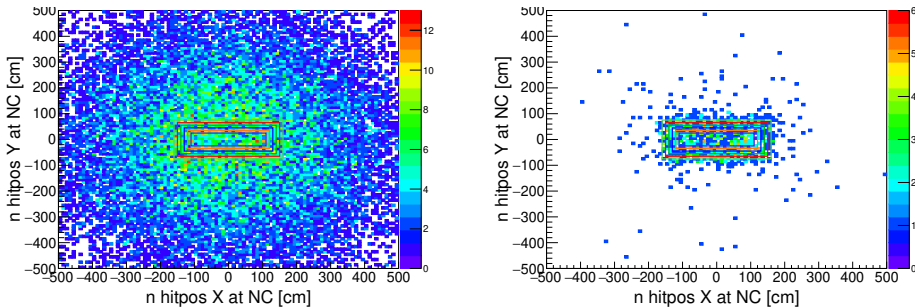


Figure 3.40: These figures show the calculated hit position at the NC from the reconstructed momentum of the  $p(K^-, \pi^+ \pi^-) n$ . The left figure indicates all events and the right figure indicates with the NC signal. The box indicates the NC size.

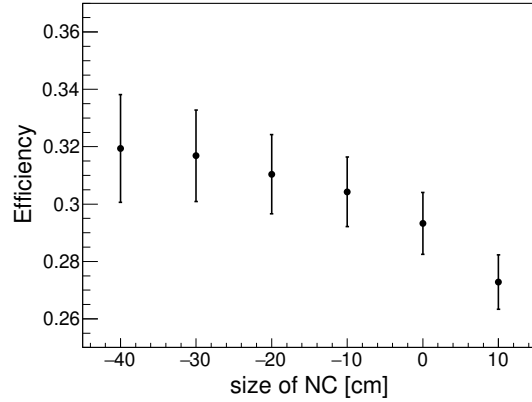


Figure 3.41: This figure indicates the relation of NC efficiencies and selected regions. Error bars represents statistic errors.

### 3.5.3 Neutron overkill by the BVC/CVC

The events with the BVC or the CVC signal was rejected as the neutral trigger. The main cause of the BVC was guessed the beam condition, for example, pill up. So, the over-veto effect due to the BVC and the CVC for the neutral trigger should be estimated using the same data of the production.

In the production run, the over-veto effect was evaluated using the unbaised  $K \otimes CDH/2$  trigger. In this estimation, the layer1 of the NC was used as the veto counter for the charged particles. Another layer was used for the measurement of neutral particles. Fig3.42 shows the  $1/\beta$  spectrum measured for this study, in which the quasi-elastic neutron events were seen. For the over-veto estimation, this quasi-elastic neutron was used, which was represents the red hatched region.

The over-veto ratio was estimated at  $0.081 \pm 0.007$  whether the BVC or the CVC have the signal.

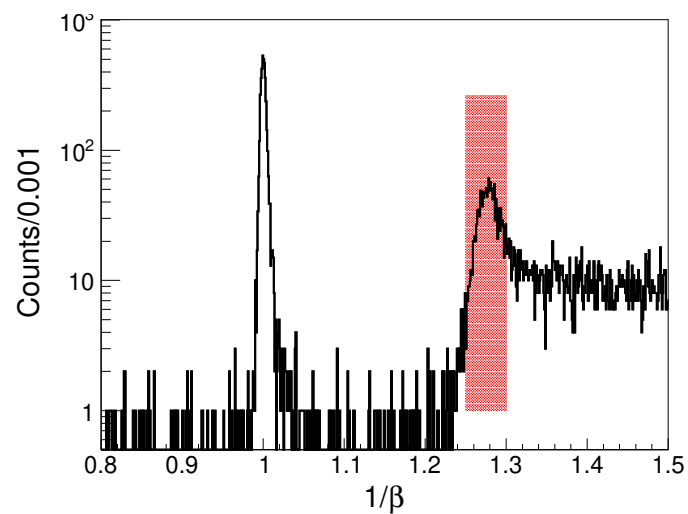


Figure 3.42: This figure shows  $1/\beta$  spectrum by layer 2~7 of the NC with NC layer 1 veto in the unbaised  $K \otimes CDH2$  trigger. The quasi-elastic peak was seen around  $\beta = 1.27$ . The red hatched region indicates an acceptable region as the quasi-elastic neutron.

# Chapter 4

## Discussion

### 4.1 $\pi\Sigma$ spectra

In this section, we first describe how to classify the  $\pi\Sigma$  modes and convert the spectra obtained from MC simulations with acceptance correction to cross sections. For forward protons, the solid angle of the forward proton detector depends on the momentum due to the beam-swept magnet. This effect is also evaluated using MC simulations.

#### 4.1.1 Mode decomposition of $d(K^-, p)$

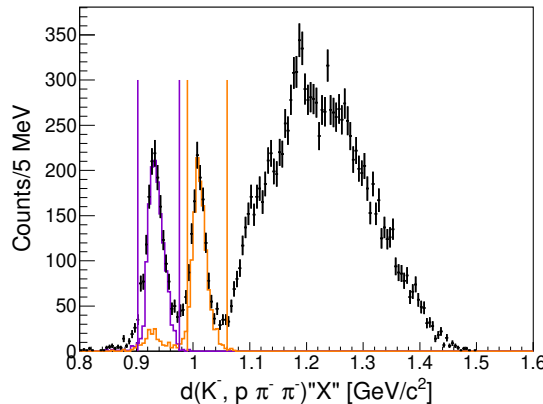


Figure 4.1: This figure shows the missing mass of  $d(K^-, p\pi^-\pi^-)$ . Orange and purple lines indicate selection region as missing  $p$  and  $p\pi^-$ , respectively.  $d(K^-, p\pi^-)\Sigma^0$  and  $d(K^-, p\pi^-)\Lambda$  tagged events are drawn orange and purple plot in same figure.

In the case of forward protons, the  $\pi^-\Sigma^0$  mode is identified from the event where two  $\pi^-$  are detected by the CDS. The  $\pi^-\Sigma^0$  mode has the

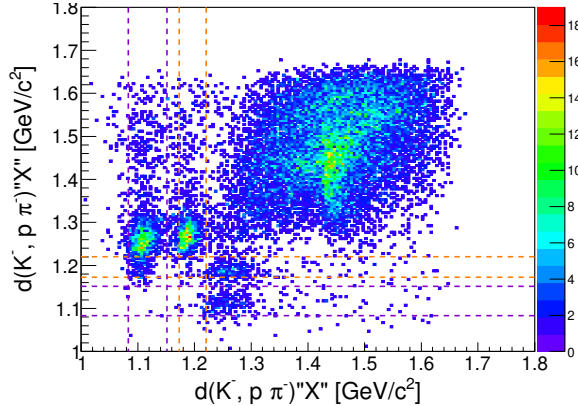


Figure 4.2: This figure shows the scatter plot of the  $d(K^-, p\pi^-)$  missing masses in the  $p$  and two  $\pi^-$  detected events. Horizontal axis represents nearer DCA  $\pi^-$  and vertical axis represents other one. Orange and purple lines indicate selection region as  $d(K^-, p\pi^-)"\Sigma^0"$  and  $d(K^-, p\pi^-)"\Lambda"$ , respectively.

following decay chain.

$$K^-d \rightarrow p\pi^-\Sigma^0 \rightarrow p\pi^-\Lambda\gamma \rightarrow p\pi^-\gamma p\pi^-$$

And  $\pi^-\Lambda$  mode has a similar decay chain.

$$K^-d \rightarrow p\pi^-\Lambda \rightarrow p\pi^-p\pi^-$$

We identify the  $\pi^-\Sigma^0$  mode by identifying  $\Sigma^0$  with  $d(K^-, p\pi^-)$  missing mass and  $p\gamma$  with  $d(K^-, p\pi^-\pi^-)$  missing mass.

The  $d(K^-, p\pi^-\pi^-)$  missing mass is plotted in the Figure.??, with the  $\Sigma^0$  identified from the  $d(K^-, n\pi^-)$  missing mass as the orange histogram and the  $\Lambda$  identified as the purple histogram. In this reaction,  $p\gamma$  make a peak like structure as this figure, because  $\pi^-\Sigma^0$  momentum is small and  $\gamma$  momentum is restricted. Therefore, not only the  $\pi^-\Lambda$  mode missin  $p$  but also the  $\pi^-\Sigma^0$  missing  $p\gamma$  can be identified, the range for each identification is represented by the purple and orange vertical lines.

#### 4.1.2 Mode decomposition of $d(K^-, n)$

In the case of forward neutrons, the missing neutron is identified from the  $d(K^-, n\pi^-\pi^+)$  missing mass as shown in the Figure.4.3, and the  $K^-d \rightarrow n\pi^-\pi^+"n"$  final state is identified. The following reactions are possible for this final state.

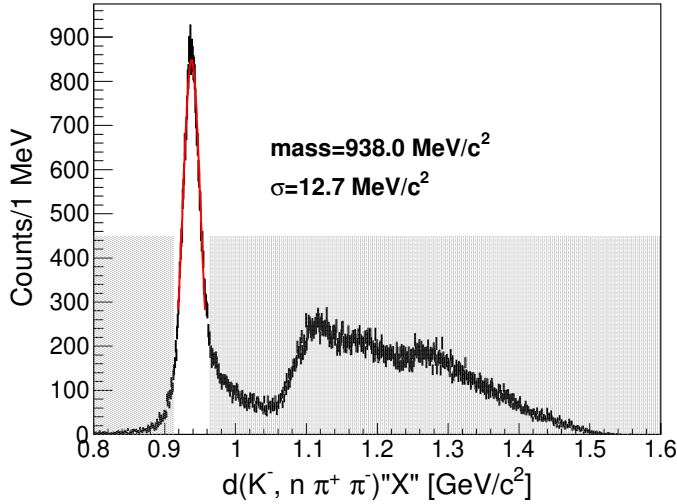


Figure 4.3: This figure shows  $d(K^-, n\pi^+\pi^-)''X''$  spectrum. Red line indicates fitting gaussian and gray hatched region indicates rejected region for  $d(K^-, n\pi^+\pi^-)''n''$  events.

$$K^- d \rightarrow K^0 nn \quad (4.1)$$

$$K^- d \rightarrow \Sigma_{forward}^+ \pi^- n \quad (4.2)$$

$$K^- d \rightarrow \Sigma_{forward}^- \pi^+ n \quad (4.3)$$

$$K^- d \rightarrow \Sigma^+ \pi^- n_{forward} \quad (4.4)$$

$$K^- d \rightarrow \Sigma^- \pi^+ n_{forward} \quad (4.5)$$

In the reaction.(4.1) of these reactions,  $K^0$  is produced and  $K^0$  decays to  $\pi^+$  and  $\pi^-$ . And the reaction.(??) and reaction.(??) produce forward charged  $\Sigma$ . The neutrons measured by the forward detector are decays from the produced  $\Sigma$ .

These three reactions can be identified by reconstructing  $K^0$  from the invariant mass of  $\pi^+$  and  $\pi^-$ ,  $\Sigma^+$  from neutron and  $\pi^+$ , and  $\Sigma^-$  from neutron and  $\pi^-$ , as shown in the Figure.??.

The remaining reactions.(4.4) and (4.5) are 2-step reactions in which the  $\bar{K}$  meson kicks the neutron forward and reacts with the residual nucleon, scattering  $\pi\Sigma$  backward, which is the signal we want to measure.

The two modes are identified by the  $d(K^-, n\pi)$  missing masses as shown in Figure.???. In that figure for example, in the case of the  $\pi^-\Sigma^+$  mode,

the missing mass of the charge opposite to  $\Sigma$  results in the correct peak as shown in the red line, while the missing mass of  $\Sigma$  decays from and is widely distributed in the kinematically allowed region without any structure as shown in the blue line.

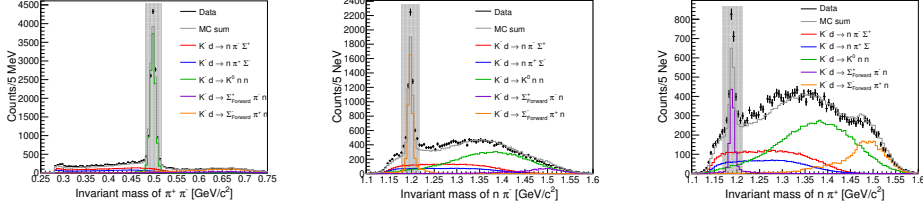


Figure 4.4: These figures shows invariant masses of  $\pi^+\pi^-$ ,  $n\pi^-$  and  $n\pi^+$  with fitting result of 5 reactions.

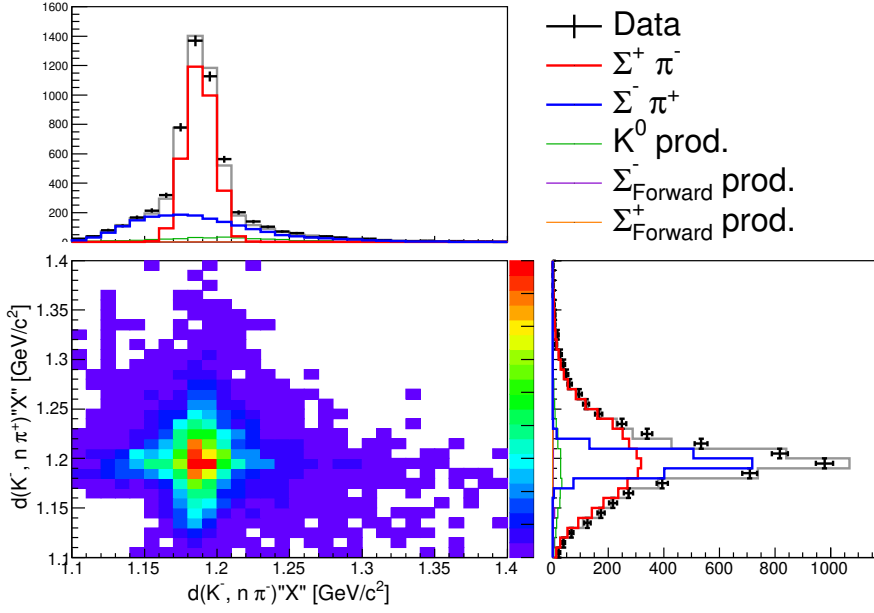


Figure 4.5: This figure indicates summed up fitting result and log-likelihood value of each bins.

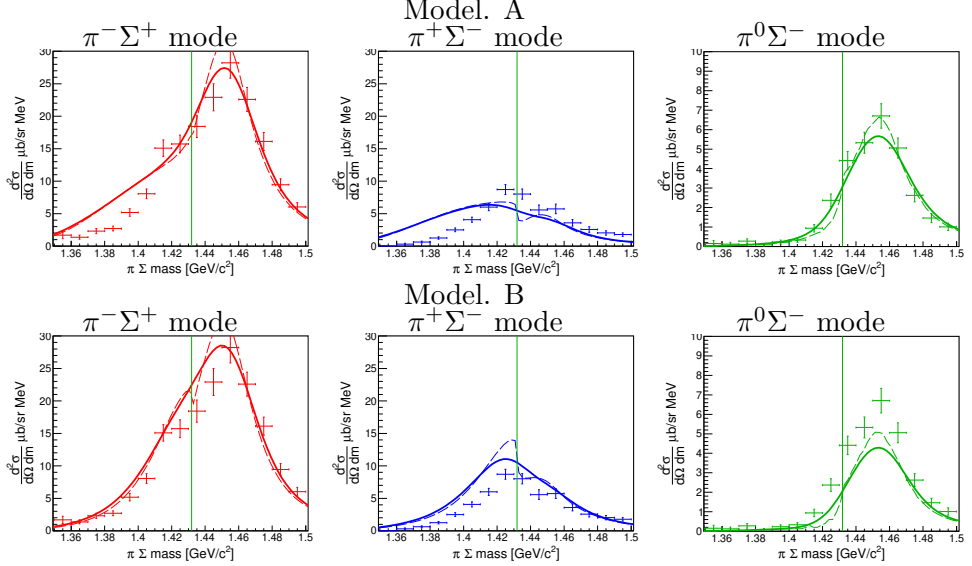


Figure 4.6: This figure shows obtained spectra and DCC calculation [44]. Error bar indicates obtained spectra. Dashed and solid line indicate theoretical calculation itself and calculation convoluted by detector resolution, respectively. Left, center and right figures represent  $\pi^- \Sigma^+$ ,  $\pi^+ \Sigma^-$  and  $\pi^0 \Sigma^-$ , respectively.

## 4.2 Comparison with DCC model

The DCC model [?] is constructed from fitting of various  $K^- p \rightarrow$  meson-baryon data from the  $\bar{K}N$  threshold to  $W = 2.1\text{GeV}/c$  as described in section, the model can treat comprehensively scattering including strangeness in wide energy region which including high energy 1-step  $K^- p \rightarrow \bar{K}N$  scattering and  $\bar{K}N \rightarrow \pi\Sigma$  scattering below the  $\bar{K}N$  threshold, however the region below the threshold is extrapolation. The theoretical calculation by the model was performed [44]. We plotted into same figure as shown in Fig.4.6. The obtained data was plotted as error bars and theoretical calculation was plotted as lines. The dashed line indicates theoretical calculation itself and the solid line indicates them convoluted by the detector resolution which shown in Fig.B.4. The overall strength of each spectra is well matched, which means this reaction mechanism seems to consider 2-step reaction of  $K^- N \rightarrow \bar{K}N$  and  $\bar{K}N \rightarrow \pi\Sigma$  is dominant as described in Sec.??.

Next, we compare with decomposed component of  $I = 1$ ,  $I = 1$  and these interference term as shown in Fig.4.7 to discuss about detail spectra shape. While interference term seems to be well matched each models, there are some difference about  $I = 0$  and  $I = 1$ , which is different part of each spectra depend on the model. In the case of  $I = 0$  channel, model.A differ about the spectrum shape. On the other hand, model.B seems to be better

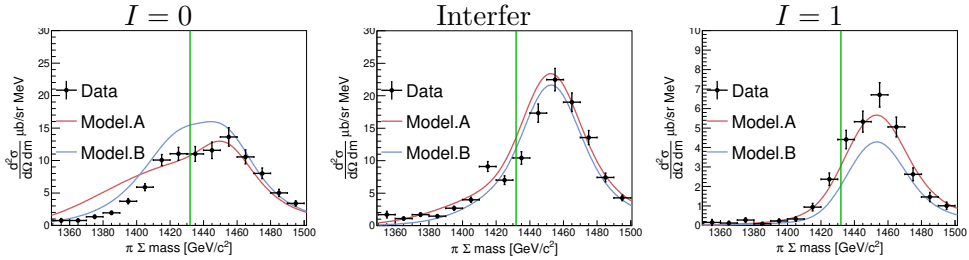


Figure 4.7: These figures show comparison with decomposed  $I = 0$ ,  $I = 1$  and these interference term. Left, center and right represent about  $I = 0$ , interference and  $I = 1$  component, respectively. Dark red and dark blue indicate model.A and model.B, respectively.

matched than model.A. The fact is considered due to large width of higher mass region pole on model.A, so model.A has a long tail component below the  $\bar{K}N$  threshold, which component can not be explain the data. Model.B is good matched about spectrum shape, but the strength of theoretical calculation is shortage.

### 4.3 Demonstration of fitting by DCC models

Next, we performed demonstration of fitting by DCC models to discuss each component how to contribute each spectra. First, we use the strength of  $I = 0$  and  $I = 1$  as free parameter, which scale  $I = 0$  and  $I = 1$  spectra. The interference term also change corespond to the isospin relation as follow rrepresentation.

$$\begin{aligned} \frac{d\sigma_{\pi^-\Sigma^+}}{dM d\Omega} &= \frac{1}{3} A_{I=0} |T_{I=0}|^2 + \frac{1}{2} A_{I=1} |T_{I=1}|^2 + \frac{2}{\sqrt{6}} \sqrt{A_{I=0} A_{I=1}} \text{Re}(T_{I=0} T_{I=1}^*) \\ \frac{d\sigma_{\pi^+\Sigma^-}}{dM d\Omega} &= \frac{1}{3} A_{I=0} |T_{I=0}|^2 + \frac{1}{2} A_{I=1} |T_{I=1}|^2 - \frac{2}{\sqrt{6}} \sqrt{A_{I=0} A_{I=1}} \text{Re}(T_{I=0} T_{I=1}^*) \\ \frac{d\sigma_{\pi^0\Sigma^-}}{dM d\Omega} &= \frac{1}{2} A_{I=1} |T_{I=1}|^2 \end{aligned} \quad (4.6)$$

Where,  $A_{I=0}$  and  $A_{I=1}$  is scaling factor introduced as 2-step scattering strength. And interference term is changed according to square root of each strength.

Fig.[4.8] shows about fitting result of Model.A, in which above figures show obtained spectra and bottom figures show calculated spectra. We note that fitting are used only above 3 spectra. At the result, we obtain  $A_{I=0} = 0.562 \pm 0.015$  and  $A_{I=1} = 1.070 \pm 0.040$  with  $\chi^2/NDF = 691/42 \sim 16.4$ . In the model.A,  $\pi^-\Sigma^0$  of  $I = 1$  is obtained good matched, that strongly affect

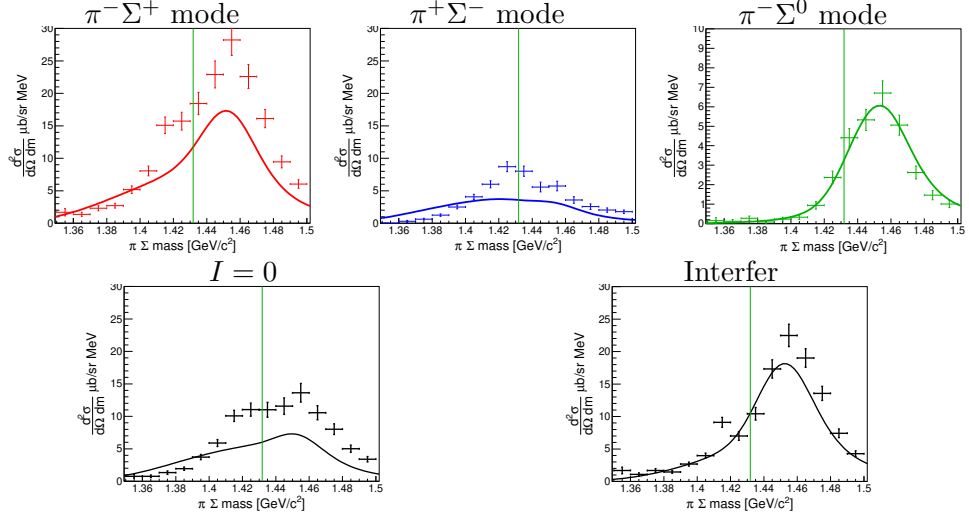


Figure 4.8: These figures show fitting result about  $A_{I=0}$  and  $A_{I=1}$  using model.A. Above figures are used fitting. Left, center and right represents  $\pi^-\Sigma^+$ ,  $\pi^+\Sigma^-$  and pure  $I = 1 \pi^-\Sigma^0$  channels. Bottom figures show calculated components. Left and right indicate  $I = 0$  and  $I = 0$  and  $I = 1$  interference. (Pure  $I = 1$  corresponds to  $\pi^-\Sigma^0$ (top right))

above the threshold, but  $I=0$  below the threshold is not matched. Therefore, the model.A can not explain obtained spectra, as shown Fig.[4.8].

On the other hand, the result of the model.B is shown as the Fig.[4.9], and the parameters are obtained at  $A_{I=0} = 0.721 \pm 0.016$  and  $A_{I=1} = 1.423 \pm 0.055$  with  $\chi^2/NDF = 220/42 \sim 5.25$ . In the model.B,  $I = 1$  strength is recovered and overall each spectra shape are matched. But, theoretical strength of  $\pi^+\Sigma^-$  is shortage above the  $\bar{K}N$  threshold. That appears in  $I = 0$  spectra.

Next, we introduce scaling factor  $B$  about interference term to study how to improve fitting and how interference term work. Then,  $\pi^-\Sigma^+$  and  $\pi^+\Sigma^-$  cross section represents as follow.

$$\begin{aligned} \frac{d\sigma_{\pi^-\Sigma^+}}{dM d\Omega} &= \frac{1}{3} A_{I=0} |T_{I=0}|^2 + \frac{1}{2} A_{I=1} |T_{I=1}|^2 + \frac{2}{\sqrt{6}} B \sqrt{A_{I=0} A_{I=1}} \text{Re}(T_{I=0} T_{I=1}^*) \\ \frac{d\sigma_{\pi^+\Sigma^-}}{dM d\Omega} &= \frac{1}{3} A_{I=0} |T_{I=0}|^2 + \frac{1}{2} A_{I=1} |T_{I=1}|^2 - \frac{2}{\sqrt{6}} B \sqrt{A_{I=0} A_{I=1}} \text{Re}(T_{I=0} T_{I=1}^*) \end{aligned} \quad (4.7)$$

Because  $\pi^-\Sigma^0$  is pure  $I = 1$  channel, we performed fitting  $I = 1$  channel is determined from only  $\pi^-\Sigma^0$ , then  $I = 0$  and the interference term decided, whose result is shown in Fig.[4.10]. The  $\chi^2/NDF = 187/41 \sim 4.56$  is improved than 5.25 of Fig.[4.9]. Parameters are  $A_{I=0} = 0.686 \pm 0.017$ ,  $A_{I=1} = 1.462 \pm 0.059$  and  $B = 0.828 \pm 0.030$  in this fitting.

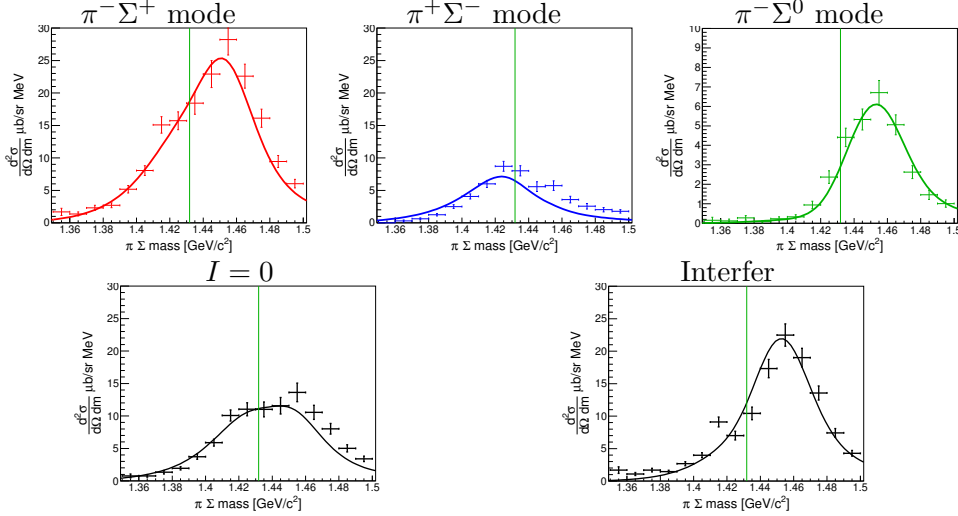


Figure 4.9: These figures show fitting result about  $A_{I=0}$  and  $A_{I=1}$  using model.B with same notation of Fig[4.8].

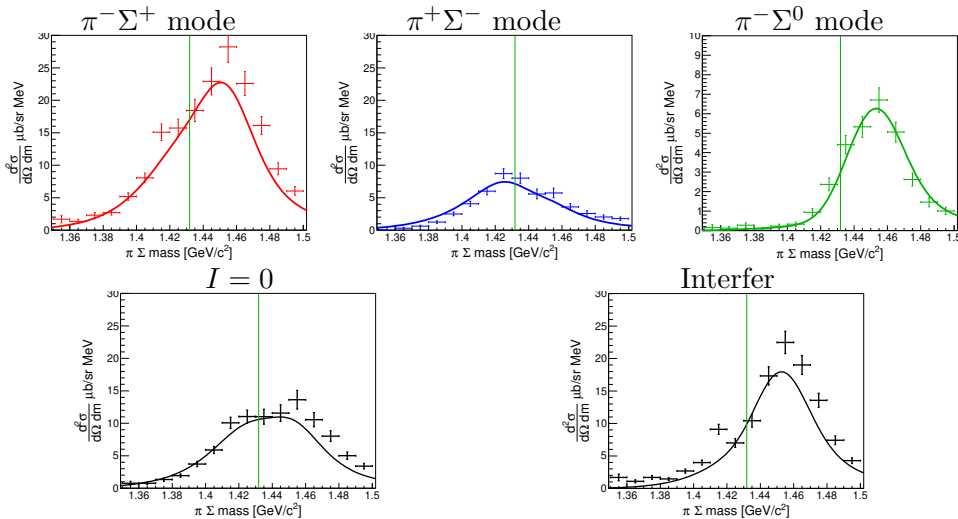


Figure 4.10: These figures shows result of the fitting, in which  $I = 1$  is decided by  $\pi^- \Sigma^0$  and  $I = 0$  and interference term are determined after. The figure notation is same as Fig.[4.8].

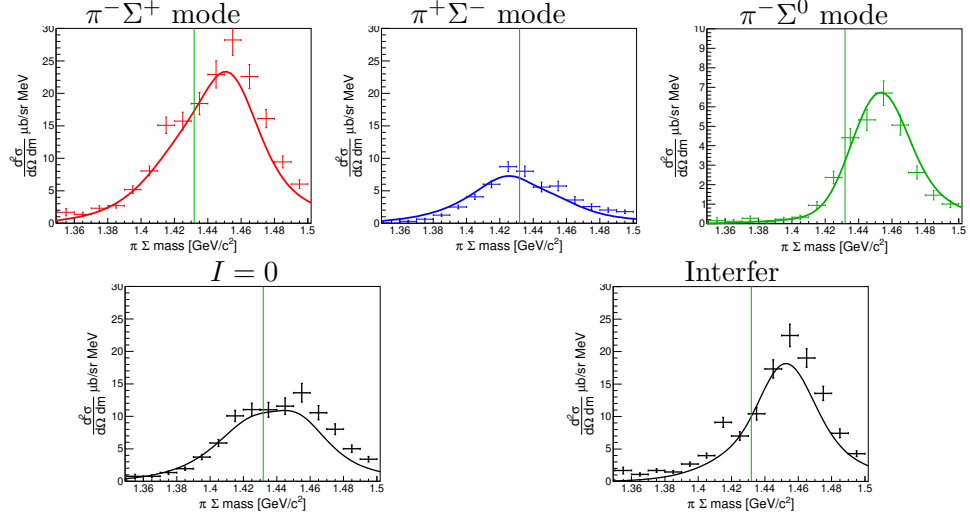


Figure 4.11: These figures show fitting result about  $A_{I=0}$ ,  $A_{I=1}$  and  $B$  that is the scaling factor about interference term using model.B with same notation of Fig[4.8].

The case of simultaneous fitting of these three parameters is shown in the Fig.[4.11], whose  $\chi^2/NDF = 184/41 \sim 4.48$  is almost same at 4.56 of the case of  $I = 1$  separately decided. Then, parameters is  $A_{I=0} = 0.682 \pm 0.017$ ,  $A_{I=1} = 1.570 \pm 0.058$  and  $B = 0.811 \pm 0.030$ .

Table.[??] lists fit parameters using the DCC model.  $I = 0$  component is scaled down to 72% and  $I = 1$  component is scaled up to 142% at fitting using  $I = 0$  and  $I = 1$  scale factor. Then the interference factor is added, the factor of  $I = 0$  component is a bit described and become to 68%, and the factor of  $I = 1$  component is increased and change to 146 – 156%. The interference term is described to 83 – 81%.

# Chapter 5

## Conclusion

We measured  $d(K^-N)\pi\Sigma$  reaction with  $1GeV/c$   $K^-$  beam at K1.8BR beamline of the hadron hall in the J-PARC as the J-PARC E31 experiment. We measured forward scattering scattering nucleon using the NC and PC. Simultaneously, decayed particles are detected by the CDS surrounding the liquid- $D_2$  target to identify final state. We identify  $K^-d \rightarrow n\pi^+\pi^-n$  final state and removed  $K^0$  and forward- $\Sigma^\pm$  production, in which forward- $\Sigma^\pm$  means forward neutron decayed from  $\Sigma^\pm$ . And, we obtain  $d(K^-, n)\pi^\mp\Sigma^\pm$ , which decomposed to  $\pi^-\Sigma^+$  and  $\pi^+\Sigma^-$  from missing mass of  $d(K^-, n\pi^\mp)\Sigma^\pm$ . We identify  $\pi^-\Sigma^0$  final state from identify  $d(K^-, p\pi^-)\Sigma^0$  and  $d(K^-, p\pi^-\pi^-)p$ . At the result, We obtained  $\pi^-\Sigma^+$ ,  $\pi^+\Sigma^-$  and  $\pi^0\Sigma^-$  cross sections from the missing mass of the  $d(K^-N)$  missing mass.

This reaction is considered as the 2-step reaction of  $K^-N \rightarrow \bar{K}N$  scattering and  $\bar{K}N \rightarrow \pi\Sigma$  scattering. 1-step reaction has large energy  $\sim 2.05GeV/c$  and 2-step can allow to occur  $\bar{K}N \rightarrow \pi\Sigma$  below the  $\bar{K}N$  threshold. Large energy 1-step reaction restricts the contamination from 1-step reaction in which a nucleon emitted as the spectator around the  $\bar{K}N$  threshold. Because the recoiled  $\bar{K}$  has low momentum  $\sim 0.25GeV/c$  around the  $\bar{K}N$  threshold, the S-wave scattering is dominant in 2-step  $\bar{K}N \rightarrow \pi\Sigma$  scattering, which is confirmed from our data not to see obvious peak around the  $\Sigma(1385)$  and  $\Lambda(1520)$ , which are P-wave and D-wave. We can understand the reaction is the above the mechanism from the matching our data and theoretical calculations which adopts or covers around high energy  $\bar{K}N$  scattering region around 1-step.

We decompose about the isospin  $I = 0$ ,  $I = 1$  and these interference term about 2-step scattering. The so-called model.B is not matched spectra shape of  $\pi^-\Sigma^+$  and  $\pi^+\Sigma^-$ , especially below the  $\bar{K}N$  threshold, because this has large width of higher pole. On the other hand, in model.B, obtained spectra are reproduced to change all  $I = 0$ ,  $I = 1$  and these interference term. That means that  $I = 0$  component is important, but  $I = 1$  component is also important even though the component does not have pole in the region

of interest. That means that  $I = 0$  component is important, but  $I = 1$  component is also important even though the component does not have pole in the region of interest. Above the threshold,  $I = 0 \pi^-\Sigma^0$  has large cross section and the interference term between  $I = 0$  and  $I = 1$  also appear as the difference of  $\pi^-\Sigma^+$  and  $\pi^+\Sigma^-$ . So, interference term is necessary to explain the these three spectra.

We obtain  $\pi^-\Sigma^+$ ,  $\pi^+\Sigma^-$  and  $\pi^-\Sigma^0$  spectra via the  $d(K^-, N)$  reaction, which is considered 2-step reaction of  $K^-N \rightarrow \bar{K}N$  and  $\bar{K}N \rightarrow \pi\Sigma$ . These spectra provide all information to determine that  $I = 0$ ,  $I = 1$  and these interference term of  $\bar{K}N \rightarrow \pi\Sigma$  scattering around the  $\bar{K}N$  threshold.

# Appendix A

## Offline selection

Decayed particles sometimes make fake trajectories and hits in the CDC and the CDH. For example, neutral particles convert to charged particles at the solenoid magnets and these make hit in the CDH. We select event by simple offline analysis to avoid these fake hits.

### A.1 $d(K^-, n\pi^+\pi^-)$

FigA.1 shows scatter plot of T0-CDH tof and energy deposit of the CDH by  $\pi^+\pi^-$  in  $n_{forward}$  and  $\pi^+\pi^-$  detected events. There are some events in slow region and low energy deposit region which will be fake events from low energy electron and decayed muon and so on. We select time window of 1–15 [ns] to reject these fake hits. FigA.2 shows energy deposit of  $\pi^+\pi^-$  in same events. Red lines indicates energy deposit summed up clustering hits. So, low energy deposit includes events that a pion pass through edge of the CDH. We select two CDH clusters event associating CDC tracks after hits filtered by time-window for  $d(K^-, n\pi^+\pi^-)$  events. We also select energy deposit of the cluster more than 4.5 [MeVee].

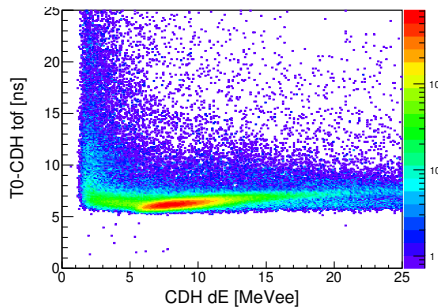


Figure A.1: The figure indicates T0-CDH tof and energy deposit of the CDH of  $\pi^+\pi^-$  hits in  $d(K^-, n\pi^+\pi^-)$  events

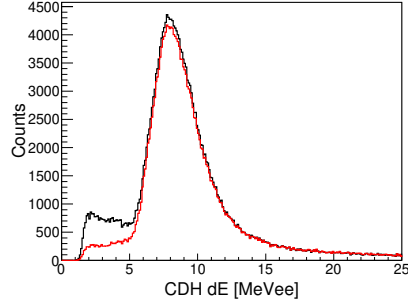


Figure A.2: This figure shows  $\pi^+\pi^-$  energy deposit of the CDH in same condition of FitA.1. Black line indicate no selection and red line indicate clustering energy deposit.

## A.2 $d(K^-, p\pi^-\pi^-)$

$d(K^-, p\pi^-\pi^-)$  event selection is same as  $d(K^-, n\pi^+\pi^-)$  event. So, CDH hits were adopted timewindow and clustering as same as  $d(K^-, n\pi^+\pi^-)$  analysis which was shown in FigA.3

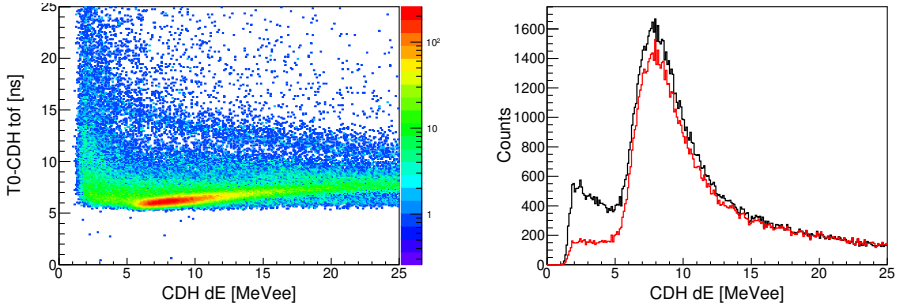


Figure A.3: These figures represent about offline selection for  $d(K^-, p\pi^-\pi^-)$  events. Left figure shows scatter plot of T0-CDH tof and CDH dE in forward proton and 2  $\pi^-$  detected events. Right figure shows CDH dE in which black line indicates without clustering and red line indicates with clustering.

## Appendix B

# Geant4 simulation

In this thesis, the Monte Carlo simulation was employed Geant4.10.01.p01 toolkit with the QGSP\_BERT\_HP physics package. This physics package adopts precompound model for high energy hadrons ( $10 - 25\text{GeV}/c$ ) which are protons, neutrons, pions, kaons and nuclei and Bertini cascade for low energy hadrons ( $\sim 10\text{GeV}/c$ ). HP means high precision for the neutron especially thermal neutron ( $< 20\text{MeV}/c$ ), so these neutrons were transported by the high precision data.

The purposes of Monte Carlo are evaluation of the acceptance of the CDS and estimation of contribution from specific reactions. 1-step reactions was simulated using previous experimental data of  $\bar{K}N$  scattering and fermi momentum, which was used to evaluate contamination to 2-step reactions in this thesis. Also, 2-step reactions was simulated as  $S$ -wave scattering, which was used to evaluated the acceptance of the CDS. In  $d(K^-, n\pi^+\pi^-)''n''$  final state, 2-step simulation of  $d(K^-, n)''\pi^\mp\Sigma^\pm$  was used to separation of each modes by template fittings. As Sec??, this final state was sucessfully decomposed to 5 reactions which are  $K^-d \rightarrow \pi^\mp\Sigma^\pm n$  (1-step),  $K^-d \rightarrow K^0nn$  (1-step) and  $K^-d \rightarrow n\pi^\mp\Sigma^\pm$  (2-step).

The result of the Monte Carlo simulation of  $d(K^-, n\pi^+\pi^-)''n''$  final state and template fitting was used for some calibrations. The CDS magnetic field was calibrated using  $K^0$  peak which was subtracted background which was shown in FigB.1. We searched correct field value value while changing the inputed field value that indicates in FigB.2. The CDC resolution was estimated at  $280\mu\text{m}$  using width of  $K^0$  peak while changing the inputed resolution.

The NC resolution was evaluated  $d(K^-, n\pi^+\pi^-)''n''$  peak which was shown in FigB.4. The  $K^-d \rightarrow n\pi + \pi^-n$  events was decomposed which described in Sec??, so red plot in FigB.4 was reproduced using the Monte Carlo samples and template fitting. The NC time resolution was estimated at  $170\text{ps}$  while changing the inputed resolution for the Monte Carlo simulation. The PC/CVC time resolution is adopted similar procedure to

$d(K^-, p\pi^-\pi^-)''p''$  peak which is come from the  $K^-d \rightarrow p\Lambda\pi^-$  scattering as shown in FigB.5.

The  $d(K^-, n)''X''$  missing mass resolution was estimated using the  $d(K^-, n)''\pi^\mp\Sigma^\pm$  Monte Carlo simulation as shown in FigB.6, so we estimated about  $10\text{MeV}/c^2$  at the  $\bar{K}N$  threshold. The resolution was given 3rd polynomial function by fitting to this figure which was shown in same figure.

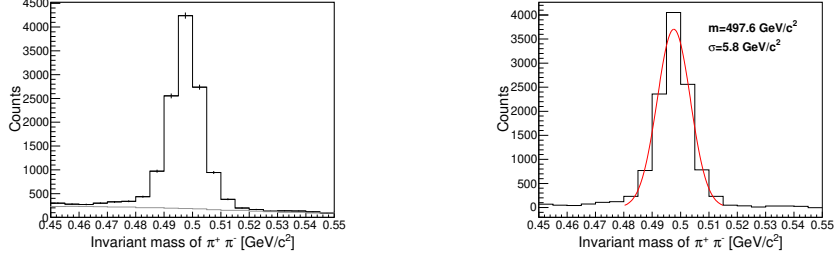


Figure B.1: Right figure shows the invariant mass of  $\pi^+\pi^-$  in the  $d(K^-, n\pi^+\pi^-)''n''$  missing masses with estimated background which was indicated as gray line. Left figure shows the  $K^0$  peak which was subtrackted spectrum with fitted Gaussian, that was red line.

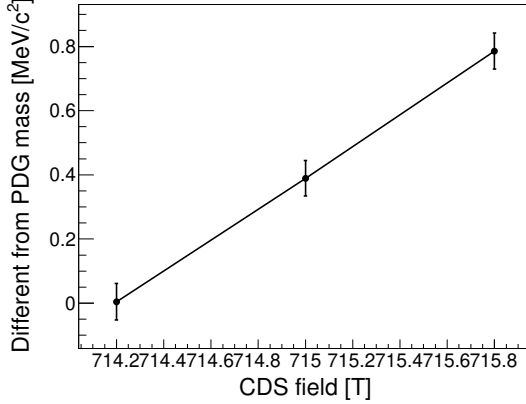


Figure B.2: This figure indicates relation of the CDS field value and  $K^0$  peak position which was indicated in left figure of FigB.1.

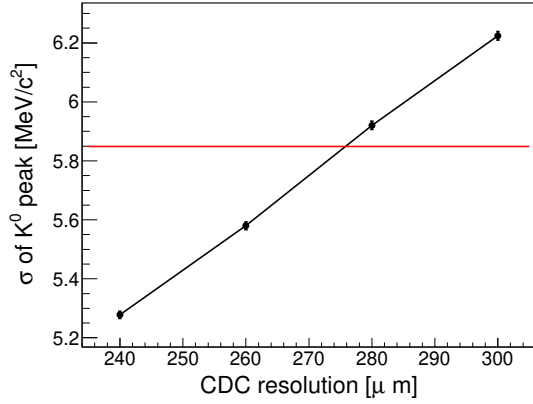


Figure B.3: This figure indicates relation of the CDC resolution and width of  $K^0$  peak. Red line indicates width of  $K^0$  peak by data which was described in left figure of FigB.1.

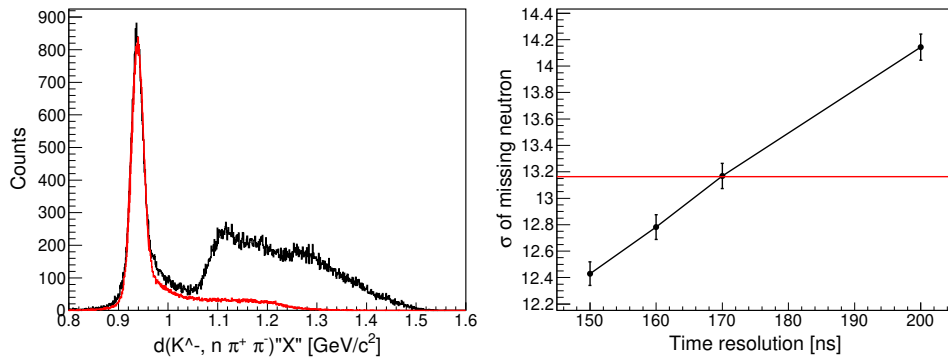


Figure B.4: Left figure shows  $d(K^-, n\pi^+\pi^-)''n''$  missing mass spectra. Black one indicates data and red one indicates the summed up Monte Carlo simulation data. Right figure indicates relation of  $\sigma$  of  $d(K^-, n\pi^+\pi^-)''n''$  peak which was estimated Gaussian fitting and inputted time resolution. Red line indicate fitting result of the data.

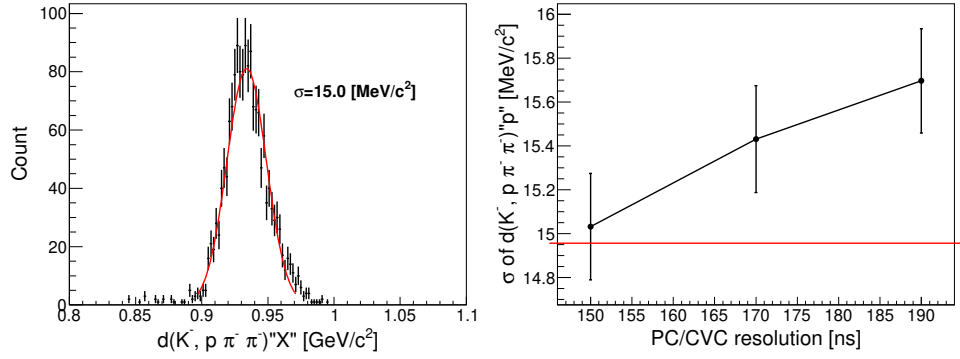


Figure B.5: Left figure shows  $d(K^-, p\pi^-\pi^-)''p''$  missing mass spectrum in  $d(K^-, p)\pi^-\Lambda$  events. Red line indicates fitting result. Right figure indicates relation of  $\sigma$  of  $d(K^-, p\pi^-\pi^-)''p''$  peak which was estimated Gaussian fitting and inputed time resolution. Red line indicate fitting result of the data.

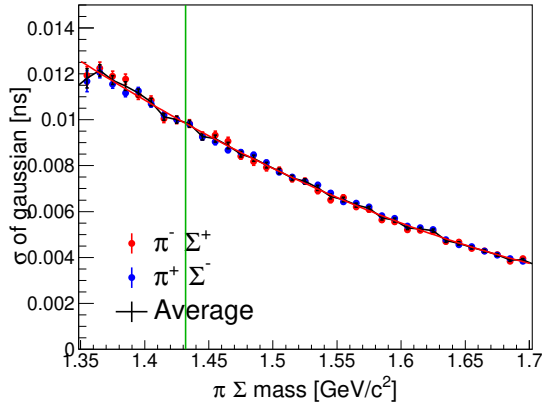


Figure B.6: This figure indicates about  $d(K^-, n)''X''$  missing mass resolution which was estimated by the  $d(K^-, n)\pi^\mp\Sigma^\pm$  Monte Carlo simulation. Red, blue and black plot indicates the  $d(K^-, n)\pi^-\Sigma^+$ , the  $d(K^-, n)\pi^+\Sigma^-$  and average of these, respectively. Fitted 3rd polynomial function is plotted at same time.

## Appendix C

### $K^- d \rightarrow K^0 nn$ events

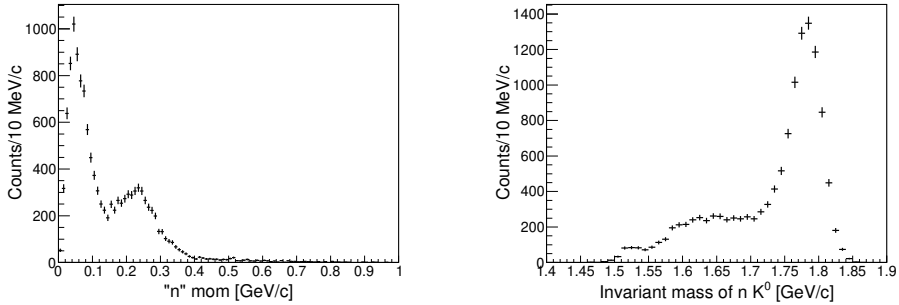


Figure C.1: Left figure indicates missing neutron momentum distribution in  $d(K^-, nK^0)"n"$  events. Right figure indicates invariant mass of  $nK^0$  in same event sample.

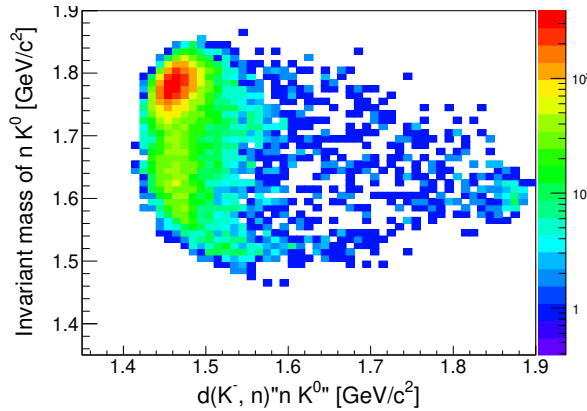


Figure C.2: This figure represents scatter plot of the  $d(K^-, n)"nK^0"$  and invariant mass of the  $nK^0$  which are detected particles.

In the  $d(K^-, n)"nK^0"$  reaction, the missing neutron momentum disribu-

tion should be corresponding to fermi motion distribution. Invariant mass distribution of  $n_{detected}K^0$  should also be distributed just below the kinematical threshold which is about  $1.8\text{GeV}/c^2$  with  $1\text{GeV}/c^2 K^-$  beam. On the other hand, the missing neutron momentum distribution was observed high momentum component and the invariant mass of  $n_{detected}K^0$  was observed widely distributed component in the data as FigC.1. Such widely distribution is not observed in the  $d(K^-, n)''nK^0''$  distribution as FigC.2.

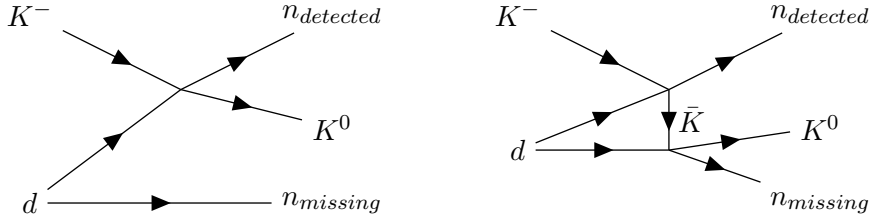


Figure C.3:

FigC.3 indicates feynmman daiagram of 1-step reaction and 2-step reaction of  $K^-d \rightarrow K^0nn$  final state.  $d(K^-, n)''nK^0''$  spectrum strongly reflects to 1-step  $\bar{K}N$  scattering, on the other hand invariant mass of  $n_{detected}K^0$  strongly reflects to interaction between recoiled  $\bar{K}$  and residual nucleon. We simulated this reaction using following simply assamption. The 1-step reaction was simulated quasi-elastic scattering of  $K^-p \rightarrow K^0n$  reaction and recoil  $K^0$  rescattered with residual nucleon isotropically. In left figure of FigC.1, a bump structure around  $\Lambda(1520)$  is seen. So, We also simulated  $K^-n \rightarrow n_{forward}\Lambda(1520)$  reaction.

We perfom fitting for invariant mass spectra to estimate ratio of 2-step like reaction. In this fitting, strength of  $\pi^\mp\Sigma^\pm$  was fixed and quasi-elastic (1-step) reaction, quasi-elastic with rescattering (2-step) reaction and  $\Lambda(1520)$  production were free parameters. Fitting result indicates left figure of FigC.4. The momentum distribution of  $n_{missing}$  and  $d(K^-, n)''nK^0''$  were also shown in same figures.

According to this fitting, we obtained that the rations of 1-step, 2-step and  $\Lambda(1520)$  production is 80%, 12% and 8% in  $K^-d \rightarrow K^0nn$  final state.

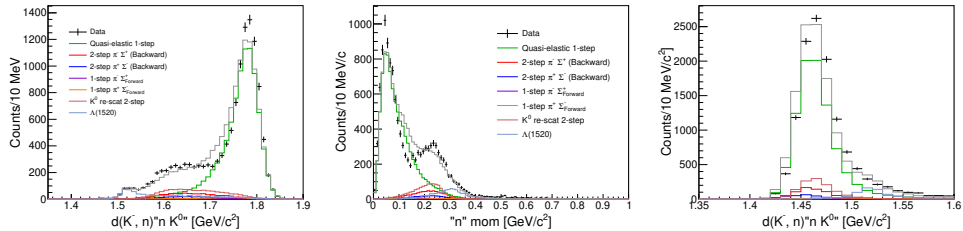


Figure C.4:

## Appendix D

### $d(K^-, p)''\pi^-\Lambda''/\pi^-\Sigma^0$ , mode

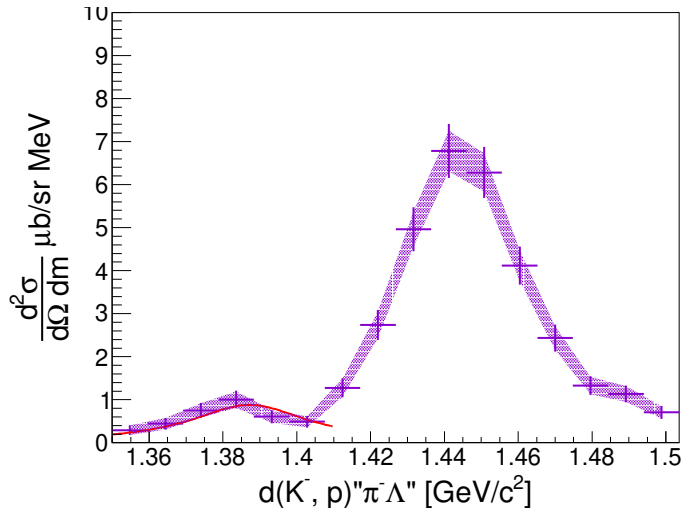


Figure D.1: This figure shows the obtained  $d(K^-, p)''\pi^-\Lambda''$  spectrum with  $\Sigma(1385)^-$  fitting which indicates as red line.

We obtain the cross section of the  $d(K^-, p)''\pi^-\Lambda''$  that is observed some structure around the  $\Sigma(1385)$  region as shown in FigD.1. Although the  $\Sigma(1385)$  whose isospin, spin and parity are  $I(J^P) = 1(3/2^+)$  is P-wave, the pole due to the  $\Sigma(1385)$  should appear 2-step effect that is constructive or destructive interference term. A constructive contribution is clearly observed in the spectrum that was fitted with fixed mass and width whose values were adopted at  $1387.2\text{MeV}/c^2$  and  $39.4\text{MeV}/c^2$  respectively that is PDG [?] value.

The  $\Sigma(1385)$  of the branching ratio of  $\pi^-\Sigma^0$  against  $\pi^-\Lambda^0$  is 0.135. The contribution to  $\pi^-\Sigma^0$  mode of this branching ratio was plotted with our obtained spectrum in FigD.2 that is almost consistent.

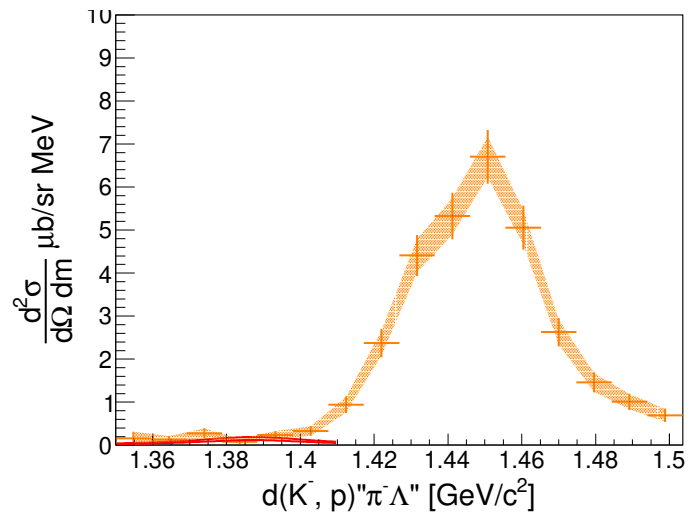


Figure D.2: This figure shows the obtained  $d(K^-, p)''\pi^-\Sigma^0''$  spectrum with  $\Sigma(1385)^-$  contribution that was estimated from  $\pi^-\Lambda$  mode.

# Bibliography

- [1] R. H. Dalitz and S. F. Tuan, Phys. Rev. Lett. 2 (1959).  
"Possible Resonant State in Pion-Hyperon Scattering"
- [2] M. H. Alston, L. W. Alvarez, P. Eberhard and M. L. Good,  
Phys. Rev. Lett. 6, 698 (1961).  
"Study of Resonances of the  $\Sigma - \pi$  System"
- [3] R. H. Dalitz, T. C. Wong and G. Rajasekaran,  
Phys Rev. **153**, 1617 (1967)  
"Model Calculation for the  $Y^*(1405)$  Resonance State"
- [4] R. J. Hemingway, Nucl Phys B **253**, 742 (1985).  
"Production of  $\Lambda(1405)$  in  $K^- p$  Reactions at 4.2GeV/ $c$ "
- [5] R. H. Dalitz and A. Deloff, J. Phys. G17, 281 (1991).  
"The Shape and Parameters of the  $\Lambda(1405)$  Resonance"
- [6] A. D. Martin, Nucl. Phys. B **179**, 33 (1981).  
"Kaon-Nucleon Parameters"
- [7] J. D. Davies et el., Phys. Lett. B **83**, 55 (1979).  
"Obserbation of Kaonic Hydrogen Atom X-rays"
- [8] M. Izyci et el., Z. Phys. A **297**, 11 (1980).  
"Results of the Search for K-series X-rays from Kaonic Hydrogen"
- [9] H. Zhang et el., Phys. Rev. C **88**, 035204 (2013).  
"Partial-wave analysis of  $\bar{K}N$  scattering reactions"
- [10] H. Zhang et el., Phys. Rev. C **88**, 035205 (2013).  
"Multichannel parametrization of  $\bar{K}N$  scattering amplitudes and extraction of resonance parameters"
- [11] P. M. Bird et el., Nucl. Phys. A **404**, 482 (1983).  
"Kaonic Hydrogen Atom X-rays"
- [12] M. Iwasaki et el., Phys. Rev. Lett. **78**, 3067 (1997).  
"Observation of Kaonic Hydrogen  $K_\alpha$  X Rays"

- [13] H. Noumi et el., Proposals for the 15th PAC meeting  
"Spectroscopic study of hyperon resonances below  $\bar{K}N$  threshold via the  $(K^-, n)$  reaction on Deuteron"
- [14] M. Bazzi et el., Phys. Lett. B **704**, 113 (2011).  
"A New Measuerment of Kaonic Hydrogen X-Rays"
- [15] Y. Ikeda, T. Hyodo, and W. Weise, Nucl. Phys. A **881**, 98 (2012)  
"Chiral SU(3) theory of antikaon–nucleon interactions with improved threshold constraints"
- [16] T. Hyodo and U.-G. Meiβner, PDG Review, Tables and Plots, Section.83  
"Pole Structure of the  $\Lambda(1405)$  Region"
- [17] T. Hashimoto et el., Phys. Rev. Lett. **128**, 112503 (2022).  
"Measurements of Strong-Interaction Effects in Kaonic-Helium Isotopes at Sub-eV Precision with X-Ray Microcalorimeters"
- [18] J. Zmeskal et el., J-PARC P57 Proposal  
"Measurement of the Strong Interaction Induced Shift and Width of the 1s State of Kaonic Deuterium at J-PARC"
- [19] G. P. Gopal et al., Nucl. Phys. B **119**, 362 (1977).  
"Partial-wave analyses of KN two-body reactions between 1480 and 2170 MeV"
- [20] N.KaiserP.B.Siegel and W.Weise, Nucl Phys A **594**, 325 (1995).  
"Chiral Dynamics and the Low-Energy Kaon-Nucleon Interaction"
- [21] D. Jido et el., Nucl. Phys. A **725**, 181 (2003).  
"Chiral Dynamics of the Two  $\Lambda(1405)$  States"
- [22] Jonathan M. M. Hall et el, Phys. Rev. Lett. **114**, 132002 (2016).  
"Lattice QCD Evidence that the  $\Lambda(1405)$ ) Resonance is an Antikaon-Nucleon Molecule"
- [23] H. Kamano et el., Phys. Rev. C **90**, 065202 (2014).  
"Dynamical Coupled-Channels Model of  $K^- p$  Reactions:  
Determination of Partial Wave Amplitudes"  
Phys. Rev. C **92**, 025205 (2015).  
"Dynamical Coupled-Channels Model of  $K^- p$  Reactions.  
Extraction of  $\Lambda^*$  and  $\Sigma^*$  Hyperon Resonances"  
Phys. Rev. C **95**, 044903(E) (2015).
- [24] L. Roca and E. Oset, Phys. Rev. C **87**, 055201 (2013).  
" $\Lambda(1405)$  poles obtained from  $\pi^0 \Sigma^0$  photoproduction data"

- [25] S. X. Nakamura and D. Jido, Phys. Theor. Exp. Phys., **2014**, 023D01 (2014).  
"Lambda (1405) photoproduction based on the chiral unitary model"
- [26] J. Esmaili, Y. Akaishi, and T. Yamazaki, Phys. Lett. B **686**, 23 (2010)  
"Experimental confirmation of the  $\Lambda(1405)$  ansatz from resonant formation of a  $K^-p$  quasi-bound state in  $K^-$  absorption by  ${}^3\text{He}$  and  ${}^4\text{He}$ "
- [27] M. Hassanvand et al., Phys. Rev. C **87**, 055202 (2013)  
"Theoretical analysis of  $\Lambda(1405) \rightarrow (\pi\Sigma)^0$  mass spectra produced in  $p + p \rightarrow p + \Lambda(1405) + p$  reactions"
- [28] J. Siebenson and L. Fabbietti, Phys. Rev. C **88**, 055201 (2013)  
"Investigation of the  $\Lambda(1405)$  line shape observed in  $pp$  collisions"
- [29] M. Niiyama et al., Phys. Rev. C **78**, 035202 (2008).  
"Photoproduction of  $\Lambda(1405)$  and  $\Sigma(1385)$  on the proton at  $E_\gamma = 1.5\text{-}2.4\text{GeV}/c$ "
- [30] M. Niiyama et al., Phys. Rev. C **78**, 035202 (2008).  
"Photoproduction of  $\Lambda(1405)$  and  $\Sigma(1385)$  on the proton at  $E_\gamma = 1.5\text{-}2.4\text{GeV}/c$ "  
J. K. Ahn, Nucl. Phys. A **721**, 715c (2002).  
" $\Lambda(1405)$  photoproduction at Spring-8/LEPS"
- [31] K. Moria for the CLAS Collaboration,  
Phys. Rev. C **87**, 035206 (2013).  
"Measurement of the  $\pi\Sigma$  photoproduction line shapes near the  $\Lambda(1405)$ "
- [32] K. Moria for the CLAS Collaboration,  
Phys. Rev. Lett. **112**, 082004 (2014).  
"Spin and parity measurement of the  $\Lambda(1405)$  baryon"
- [33] J.C.Nacher et al., Phys. Lett. B **455**, 55 (1999).  
"Photoproduction of the  $\Lambda(1405)$  on the proton and nuclei"
- [34] G. Agakishiev for the HADES Collaboration,  
Phys. Rev C **87**, 025201 (2013).  
"Baryonic Resonances to the  $\bar{K}N$  threshold: The case of  $\Lambda(1405)$  in  $pp$  collisions"
- [35] A. Cieplý and J. Smejkal, Nucl. Phys. A **881**, 115 (2012).  
"Chirally motivated  $\bar{K}N$  amplitudes for in-medium applications"
- [36] L.Fabbietti et al., Nucl. Phys. A **914**, 60 (2013).
- [37] O. Braun et al., Nucl. Phys. B **129**, 1 (1977).  
"New Information About the Kaon-Nucleon-Hyperon Coupling Constants  $g(KN\Sigma(1197))$ ,  $g(KN\Sigma(1385))$  and  $g(KN\Lambda(1405))$ "

- [38] D. Jido, E. Oset and T. Sekihara, Eur. Phys. J. A **42**, 257 (2009).  
"Kaonic Production of  $\Lambda(1405)$  off deuteron target in chiral dynamics"
- [39] K. Miyagawa, J. Haidenbauer, and H. Kamada Phys. Rev. C **97**, 055209 (2018)  
"Faddev approach to the reaction  $K - d \rightarrow \pi\Sigma n$  at  $p_K = 1.0 GeV/c$ "
- [40] S. Kawasaki et al., JPS Conf. Proc. **13**, 020018 (2017).  
"Spectroscopic Experiment of  $\Lambda(1405)$  via the In-flight  $d(K^-, n)n$  Reaction at J-PARC K1BR.8"
- [41] E. Oset, A. Ramos, and C. Bennhold, Phys. Lett. B **527**, 99 (2002);  
**530**, 260(E) (2002).  
"Low lying  $S = -1$  excited baryons and chiral symmetry"
- [42] H. Zhang, et el., Phys. Rev. C **88**, 035204 (2013). "Partial-wave analysis of  $\bar{K}N$  scattering reactions"
- [43] S. Ohnishi et el, Phys. Rev. C **93**, 025207 (2016).  
"Strcture of the  $\Lambda(1405)$  and the  $K^-d \rightarrow \pi\Sigma n$  reaction"
- [44] H. Kamano et el., Phys. ReV. C**94**, 065205 (2016).  
"Toward Establishing Low-Lying  $\Lambda$  and  $\Sigma$  Hyperon Resonances with the  $\bar{K} + d \rightarrow \pi + Y + N$  Reaction"
- [45] T. Hyodo and D. Jido, Prog. Part. Nucl. Phys. **67**, 55 (2012).  
"The Nature of the  $\Lambda(1405)$  Resonace in Chiral Dynamics"
- [46] K. Agari et el, Prog. Theor. Exp. Phys., 02B009 (2012)
- [47] K. Agari et el, Prog. Theor. Exp. Phys., 02B011 (2012)
- [48] TRANSPORT <http://linac96.web.cern.ch/Linac96/Proceedings/Thursday/THP72/Paper.pdf>
- [49] T. K. Ohska et al., Nuclear Science, IEEE Transactions on **33**, 98 (1986).
- [50] M. Shiozawa and et el., A new TKO system manager board for a dead-time-free data acquisition system, in 1994 IEEE Nuclear Science Symposium-NSS'94, pages 632–635, (1994)
- [51] M. Iio et al., Nucl. Instrum. Methods Phys. Res., Sect. **A** **687**, 1 (2012).
- [52] S. Agostinelli et al., Nucl. Instrum. Methods Phys. Res., Sect. **A** **506**, 250 (2003)  
J. Allison et el., IEEE Transactions on Phys. Sci. **53**, 207 (2006)  
J. Allison et al., Nucl. Instrum. Methods Phys. Res., Sect. **A** **835**, 186 (2016)
- [53] K. Fuji, [https://www-jlc.kek.jp/subg/offl/lib/docs/helix\\_manip/node3.html](https://www-jlc.kek.jp/subg/offl/lib/docs/helix_manip/node3.html) (1968).

- [54] Opera Electromagnetic FEA Solution Software
- [55] V. Flaminio et al., CERN-HARA-87-01, 121 (1983).
- [56] M.Jones et el, Nucl. Phys. B **90**, 349 (1975)
- [57] R. Barlow and C. Beeston, Comp. Phys. Comm. **77**, 219 (1993).
- [58] A. Nappi, Comp. Phys. Comm. **180**, 269 (2009).
- [59] M. jones, R. Levi, Setti, D. Merrill and R. D. Tripp, Phys. Rev. B**90**, 349 (1975).
- [60] M. Bernheim and et. el., Nucl. Phys. A**365**, 349, (1981).
- [61] R. Machleidt, Phys. Rev. C**63**, 024001 (2001).
- [62] S. Agostinelli et al., Nuclear Instruments and Methods in Physics Research Section A: Accelerators, Spectrometers, Detectors and Associated Equipment **506**, 250 (2003).  
J.Allison et el., Nuclear Instruments and Methods in Physics Research Section A: Accelerators, Spectrometers, Detectors and Associated Equipment **835**, 186 (2016).